國 立 交 通 大 學

材料科學與工程學系碩士班

碩士學位論文

準分子雷射處理對於二氧化鈦奈米管陣列之型態與結構之影響

Structural and morphological transformation of titania nanotube arrays

induced by excimer laser treatment

研 究 生：阮文勝

指導教授：呂志鵬　博士

中 華 民 國 九 十 九 年 八 月

準分子雷射處理對於二氧化鈦奈米管陣列之型態與結構之影響

Structural and morphological transformation of titania nanotube arrays induced by excimer laser treatment

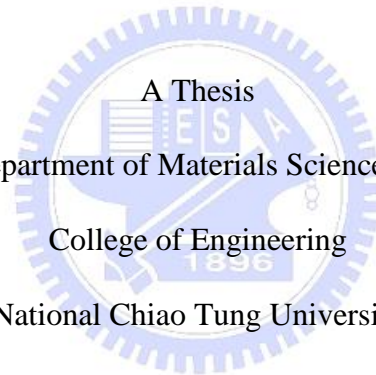研 究 生：阮文勝   Student: Nguyen Van Thang

指導教授：呂志鵬　博士   Advisor: Dr. Jihperng (Jim) Leu

國立交通大學

材料科學與工程學系

碩士論文

A Thesis

Submitted to Department of Materials Science and Engineering

College of Engineering

National Chiao Tung University

In partial Fulfillment of the Requirements

for the Degree of

Master

in

Materials Science and Engineering

August, 2010

Hsinchu, Taiwan, Republic of China

中 華 民 國 九 十 九 年 八 月

準分子雷射處理對於二氧化鈦奈米管陣列之型態與結構之影響

研 究 生：阮文勝　　　　　指導教授：呂志鵬　博士

國立交通大學

材料科學與工程學系碩士班

摘要

結晶型二氧化鈦奈米管陣列(TNAs)近年來受到廣大的矚目與應用；其中在各種結晶技術中，準分子雷射退火由於其快速與低溫的特性，而成為受重視的退火技術。而在此研究中，將對於雷射退火之功率(fluence) 與頻率 (number of laser pulses)等退火條件對於二氧化鈦奈米管陣列的結晶性，表面形態和電子架構進行研究與討論。

在此研究中，以 0.5 wt% NH_4F 和 3 wt% H_2O 的乙二醇(ethylene glycol, EG)溶液為電解質，進行陽極處理以形成高深寬比的二氧化鈦奈米管陣列。實驗在室溫下使用兩個電極式電化學系統(陰極為 SS304 不鏽鋼),在 20V 恆定的直流電壓為反應 24 小時。之後，在室溫與大氣下進行二氧化鈦奈米管陣列之準分子雷射退火。處理完之樣品將以 X 光繞射 (XRD)、掃描電子顯微術(SEM) , X 光近緣結構(XANES) 與以及拉曼光學進行材料分析與討論。

XRD 結果顯示準分子雷射之頻率少於 9000 shots，在功率為 0.067 和 0.133 Jcm^{-2} 之間所形成的 TNAs 為 anatase 相，當從 0.133 Jcm^{-2} 增加到 0.4 Jcm^{-2} 時，TNAs 的相轉變成 anatase 和 rutile 相。另外，TNAs 以雷射在 0.1 Jcm^{-2} 的功率下，頻率少於 9000 時

將從非晶相改變到 anatase。換句話說，當頻率比 9000 高時，在 TNAs 上的雷射退火從非晶相轉變到 anatase 和 rutile 相。FESEM 表面型態顯示 TNAs 表面的損害隨著功率增加與頻率增加而更加嚴重。經由上述結果，雷射所引起的相轉變機制將以雷射理論和結晶動力學來討論。另外，TNAs 結晶像的定量分析將使用 XRD 結果與理論加以計算與討論。此外，我們將提出一種新實驗方式來降低表面損壞和改進準分子雷射並增加的 TNAs 的結晶性. 最後，在此研究中，以準分子雷射進行二氧化鈦奈米管陣列退火處理功率在大於或等於 0.042 Jcm^{-2} 時，較低的價數：二價(TiO)以及三價(Ti$_2$O$_3$)也會因退火處理轉變成四價(TiO$_2$) 。

Structural and morphological transformation of titania nanotube arrays induced by excimer
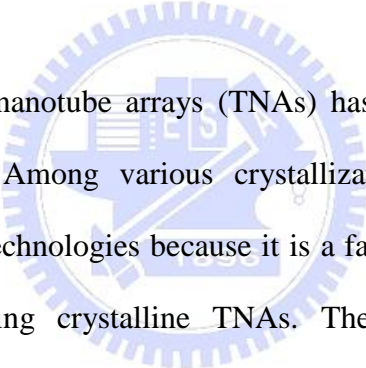laser treatment

Student: Nguyen Van Thang   Advisor: Dr. Jihperng (Jim) Leu

Department of Materials Science and Engineering

National Chiao Tung University

Abstract

Crystallization of TiO_2 nanotube arrays (TNAs) has received extensive interest for their attractive applications. Among various crystallization techniques, excimer layer annealing is one of prominent technologies because it is a fast and effective low-temperature annealing technique for forming crystalline TNAs. The influence of laser annealing conditions such as fluence and number of laser pulses on the crystallinity, surface morphology and electronic structure of TNAs were investigated.

In this study, TiO_2 nanotube arrays with high aspect-ratio have been prepared by anodic oxidation in an electrolyte including ethylene glycol, 0.5 wt% NH_4F, and 3 wt% H_2O. All anodization experiments were carried out at room temperature using a two-electrode electrochemical cell consisting of a stainless steel foil (SS304) as the cathode and a Ti foil as the anode, at constant DC potential at 20 V for 24 hours. Subsequently, TNAs were irradiated by laser in air at room temperature. Samples are analyzed using following techniques: X-Ray Diffraction (XRD), Scanning Electron Microscopy (SEM), X-Ray Near Edge Spectroscopy (XANES), and Raman Spectroscopy.

The XRD results show that TNAs annealed by laser at fluence between 0.067 and 0.133 Jcm^{-2} under 9000 shots yield anatase phase, while at fluence from 0.133 to 0.4 Jcm^{-2}, 9000 shots, TNAs possess both of anatase and rutile phases. In addition, TNAs annealed by laser at fluence of 0.1 Jcm^{-2} and shots less than 9000 will be transformed from amorphous to anatase. On the other hand, when shots are higher than 9000, laser annealing on TNAs leads to phase transformation from amorphous to anatase and rutile. FESEM images show that damage of TNAs surface increases with increasing fluence as well as the number of shots. Moreover, the mechanism for laser-induced structural transformation will be proposed in terms of laser-matter theory and crystallization kinetics. In addition, the phase composition of TNAs has been calculated based on XRD results and the matrix flushing method. Then, a new experimental mode was designed to reduce the surface damage as well as improve the crystallinity of TNAs induced by ELA. Finally, ELA process with fluences at 0.042 Jcm^{-2} or above results in all of lower charge state Ti^{+2} (TiO) and Ti^{+3} (Ti_2O_3) of Ti cations transferred toTi^{4+} (TiO_2). The physical mechanisms responsible for this conclusion were proposed.

Acknowledgements

Contents

Table Captions

Figure Captions

Abbreviations

ELA: Excimer Laser Annealing

TNAs: Titania Nanotube Arrays

XRD: X-ray Diffraction

SEM: Scanning Electron Microscopy

XAS: X-ray Absorption Spectroscopy

XANES: X-ray Absorption Near Edge Structure

A: Anatase

R: Rutile

Chapter 1 Introduction

On a technological point of view, TiO_2 material presents a lot of interest because of its wide range of applications, including photocatalytic devices [1], electrochromic [2], sensors [3], and dye-sensitized solar cell (DSSC) application [4]. The applications of TiO_2 are primary determined by its properties, such as crystallite structure, specific area, particle size, porosity and thermal stability. In recent years, various forms of nanostructure TiO_2, such as nanoparticles, nanorods, nanowires and nano-tubes, have attracted significant research interest [5-6]. Nano-tubes arrays have a higher specific surface area than nanowires or nanorods of 1-D structure due to the additional surface area. In this research, TiO_2 nano-tubes were developed by anodic oxidization. The first report on electrochemical anodization was given by Zwilling et al. [7] with nano-tube arrays up to a length of 500nm (10:1 aspect ratio) grown in a HF-based aqueous electrolyte. Besides, several neutral electrolytes also have recently been employed to prepare anodized titania nano-tubes with higher aspect ratio [8-9]. These studies have shown that high-aspect-ratio, self-organized TiO_2 nano-tubes with 100:1 aspect ratio could be obtained from ethylene glycol solution.

In addition, focusing on photocatalytic applications, anatase TiO_2 has the highest specific surface area among the TiO_2 structural phases (rutile, anatase, brookite) making anatase TiO_2 the most desired structure [10]. Furthermore, anatase TiO_2 with higher crystalline is preferred for photocatalysis, because higher crystalline means fewer defects for the recombination of electrons and holes [11-12]. Hence, many research efforts have focused on how to control the TiO_2 crystallite structures. Post-annealing treatment has been often used to transform amorphous TiO_2 to crystalline phases [13-14]. Yet, conventional annealing by means of furnace, which typically takes minutes to hours to obtain phase transition at high temperature around $600^{o}C$, cannot be used in low-temperature processing [15]. Thus, there is still a need to develop a technology to optimize the structural phase of TiO_2 at low-

temperature for applications such as flexible devices or sensors. Excimer laser annealing (ELA) technique is one of the preferred low temperature processing technologies for several advantages [16-26]. First, the treatment time using ELA technique is in the 25 ns range for TiO_2 transformation, which is ten orders of magnitude faster than the conventional annealing method. Second, under treatment by ELA, large amount impurities of TiO, and Ti_2O_3 inside as-grown TNAs prepared by anodic oxidation in NH_4F solution have found to be converted to TiO_2. Third, ELA offers selective absorption and low processing temperature [16-18], so it has been widely used in the semiconductor technology. For instance, laser annealing has gained interest for the fabrication of ferroelectric thin films at low the temperature and short duration of treatment [19]. In addition, laser annealing of $Pb(Zr, Ti)O_3$ (PZT), $PbTiO_3$ (PT), $SrTiO_3$, $SrBi_2Ta_2O_9$ (SBT) thin films showed that the thin films could be crystallized at a lower temperature and have a good dielectric properties [20-24]. Poly-Si thin film transistors (TFTs) also can be formed on glass substrates by using excimer laser annealing without thermal damage [25], etc. Finally, ELA might improve electrical properties of TiO_2 [26].

In this thesis, the microstructures and impurities of TiO_2 nanotube arrays induced by ELA were investigated as a function of laser annealing conditions including fluence and shots. The mechanism of phase transformation, impurities evolution and the surface morphology modification of TNAs induced by laser irradiation were examined and proposed. After that a new experimental mode was designed and carried out to eliminate the surface damage as well as improve the crystallinity of TNAs induced by ELA. In addition, the phase composition of TNAs has been calculated based on XRD results and the matrix flushing method. Finally, the effect of ELA on the charge transfer for Ti cations from lower charge state Ti^{+2} and Ti^{+3} of impurities TiO and Ti_2O_3 to Ti^{4+} (TiO_2) is investigated by using X-ray absorption near-edge structure spectroscopy (XANES). Physical mechanisms responsible for their difference in XANES spectra of different polymorphs of TiO_2 were proposed.

This thesis consists of five chapters. Chapter 1: Introduction, Chapter 2: Literature Review, Chapter 3: Experimental Techniques, Chapter 4: Results and Discussion, and Chapter 5: Conclusions and Suggestions for Future Work.

Chapter 2 Literature Review

2.1 Introduction of TiO$_2$ Materials

2.1.1 Crystal Structure, and Properties of Titanium Dioxide

Titanium dioxide, also known as titanium (IV) oxide or titania, is the naturally occurring oxide of titanium, chemical formula TiO$_2$. Titanium dioxide may exist in amorphous or polycrystalline structure. Titanium dioxide occurs in nature as well-known minerals rutile, anatase and brookite. The structures of rutile, anatase and brookite can be discussed in terms of (TiO$_6^{2-}$) octahedrals. The three crystal structures differ by the distortion of each octahedral and by the assembly patterns of the octahedral chains. Anatase can be regarded to be built up from octahedrals that are connected by their vertices, in rutile, the edges are connected, and in brookite, both vertices and edges are connected (Figure 2-1). However, only rutile and anatase are commercially important. In bulk form and with a large crystallite size, rutile is the thermodynamically stable form at normal pressure and at all temperatures up to its melting point. With a very small crystallite size, anatase is shown to be the stable form. Anatase is the usual product in inorganic syntheses. Anatase formation from an amorphous solid is reported to occur at around 400-450°C [27, 28, 29], and direct synthesis from a molecular precursor in solution is common knowledge [30]. The anatase to rutile transformation is a metastable to stable transition which has been studied for some decades [31, 32]. There is no unique transformation temperature but in the experimental studies the transition has occurred at 400-1000°C with the rate and ignition temperature being critically dependent on synthesis conditions. However, a transition temperature of 600°C at normal pressure for bulk TiO$_2$ was presented in the experimental phase diagram [33]. Properties of the important TiO$_2$ polymorphs of rutile and anatase are presented in Table 2-1 [34, 35].
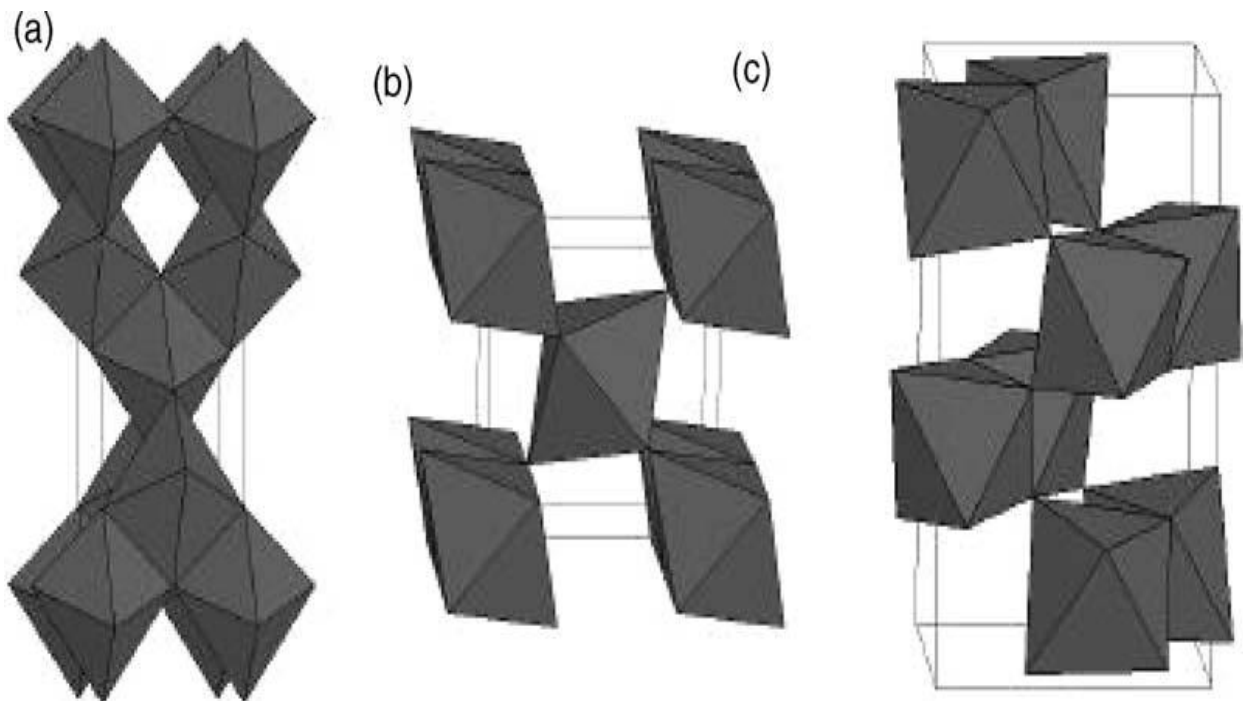
Figure 2-1   Crystal structures of (a) anatase, (b) rutile, and (c) brookite

Table 2-1   TiO$_2$ rutile and anatase structures and physical properties [34, 35]

Property	Rutile	Anatase
Crystal structure	Tetragonal	Tetragonal
Space group	P4$_2$/mnm	I4$_1$/amd
Lattice spacing a//c (nm)	0.459//0.296	0.378//0.951
Density (g/cm3)	4.26	3.89
Refract. index, 550 nm	2.75	2.54
Band gap (eV)	3.2	3.5
Melting point (℃)	1830–1850	Convert to rutile

2.1.2 Review on TiO$_2$ nanotube Arrays: Fabrication, Properties, and Applications

In recent years, nanostructural TiO$_2$ is one of the most widely studied materials due to its unique and excellent properties in optics, electronics, photochemistry and biology, as well as its applications in photovoltaic cells, sensors, and photocatalysis [36–38]. Among the various forms of nanostructural TiO$_2$ such as nanoparticles, nanorods, nanowires and nano-tubes, TiO$_2$ nano-tubes arrays has attracted increasing interest due to its highly ordered structure, high specific surface area and the convenient controlling of the size. Fabrication, properties, and applications of TiO$_2$ nanotubes have been reviewed, and the highly ordered TiO$_2$ nanotube arrays made by anodic oxidation in fluoride-contained electrolytes highlighted. The first report on electrochemical anodization was given by Zwilling et al. [7] with nano-tube arrays up to a length of 500nm (10:1 aspect ratio) grown in a HF-based aqueous electrolyte. Besides, several neutral electrolytes also have recently been employed to prepare anodized titania nano-tubes with higher aspect ratio [8-9]. These studies have shown that high-aspect-ratio, self-organized TiO$_2$ nano-tubes with 100:1 aspect ratio could be obtained from ethylene glycol solution.

The mechanism of TiO$_2$ nannotube arrays formation is presented as following. As the anodization started, the initial oxide layer [39], formed due to interaction of the surface Ti^{4+} ions with oxygen ions (O^{2-}) in the electrolyte, can be seen to homogeneously spread across the surface. At the anode oxidation of the metal releases Ti^{4+} ions and electrons, shown as [40]:

$$Ti + H_2O = TiO_2 + 2H^+ + 4e^- \qquad (1)$$

At the cathode hydrogen evolution occurs:

$$8H^+ + 8e^- = 4\ H_2 \qquad (2)$$
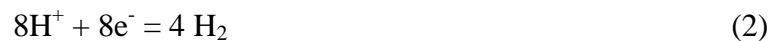
The overall process of oxide formation is given by:

$$Ti + 2H_2O = TiO_2 + 2H_2 \qquad (3)$$

The ions being mobile in the anodic layer under the applied electric field react with Ti^{4+} as described by [41]:

$$TiO_2 + 6F^- + 4H^+ = TiF_6^{2-} + 2H_2O \qquad (4)$$

$$Ti(OH)_4 + 6F^- = TiF_6^{2-} + 4OH^- \qquad (5)$$

$$Ti^{4+} + 6F^- = TiF_6^{2-} \qquad (6)$$
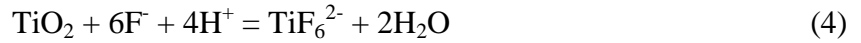
Schematic diagram of nanotube evolution at constant anodization voltage is illustrated in Figure 2-2. As seen in Figure 2-2 (b) , small pits formed due to the localized dissolution of the oxide as represented by the (4), act as pore forming centers, after which these pits convert into pores with increasing pore density, uniformly, over the surface (Figure 2-2 (c)). The pore growth occurs due to the inward movement of the oxide layer at the pore bottom (barrier layer) [39, 43]. As the pores grow deeper the electric field in these protruded metallic regions increases, enhancing field assisted oxide growth and oxide dissolution, and hence inter-pore voids start forming (Figure 2-2 (d)). Both voids and tubes grow in equilibrium. The thickness of the tubular structure stops increasing when the chemical dissolution rate of the oxide at the mouth of the tube becomes equal to the rate of inward movement of the metal/oxide boundary at the base of the tube. Higher anodization voltages increase the oxidation and field-assisted dissolution and hence, a greater nanotube layer thickness can be achieved before equilibrating with chemical dissolution.
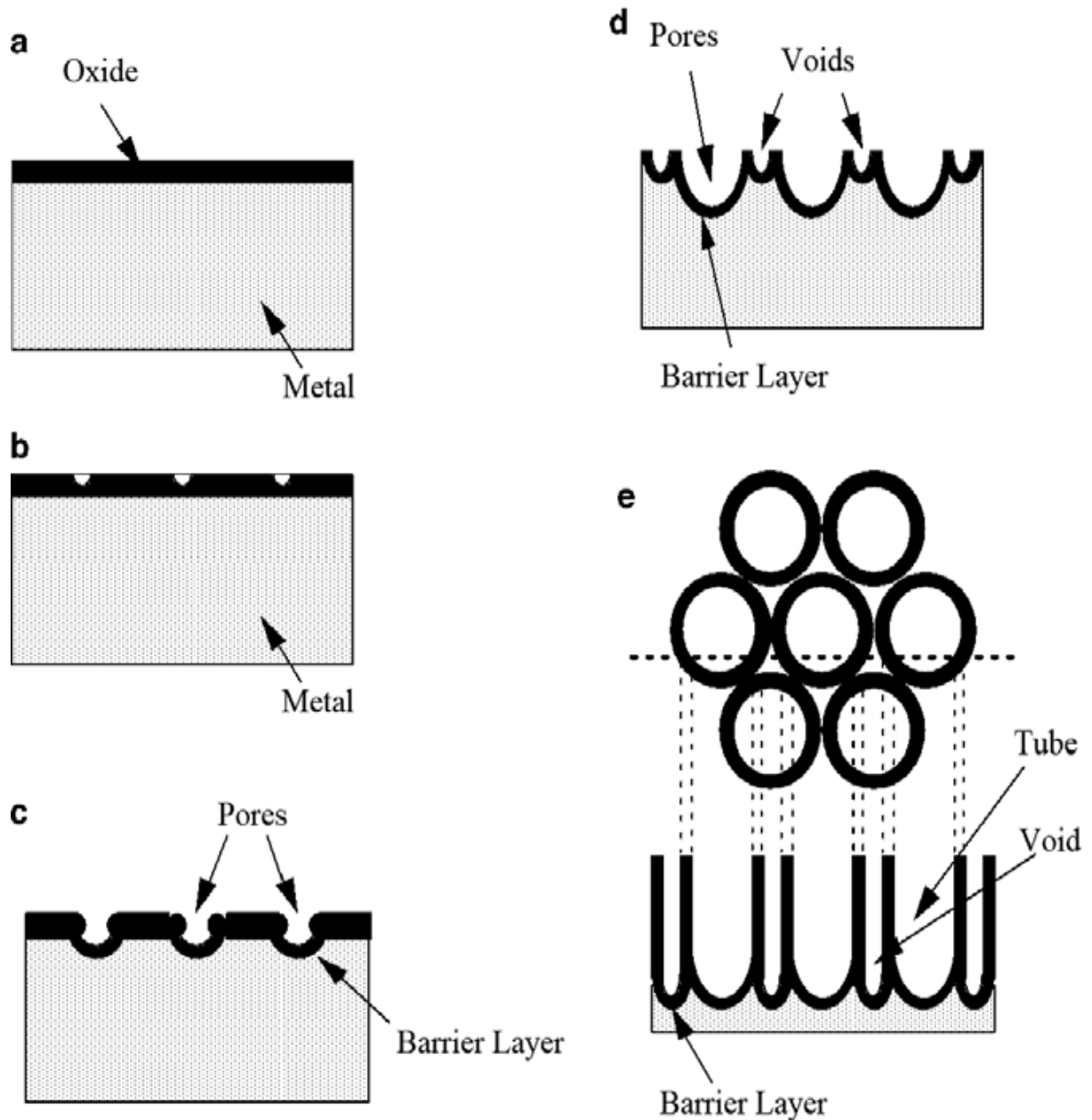
Figure 2-2   Schematic diagram of nanotube evolution at constant anodization voltage: (a) Oxide layer formation, (b) pit formation on the oxide layer, (c) growth of the pit into scallop shaped pores, (d) the metallic region between the pores undergoes oxidation and field assisted dissolution, and (e) fully developed nanotubes with a corresponding top view [42]

The excellent biocompatibility of TiO_2, the high orientation, the large surface area with tunable pore sizes, as well as the high electron transfer rate along with the nanotubes

make TiO$_2$ nanotube arrays an ideal substrate for a lot of applications. TiO$_2$ nanotubes can use in photocatalytic devices [1], electrochromic [2], sensors [3], dye sensitized solar cells [4]. Furthermore, the nanotube arrays have demonstrated great utility in biomedical related applications including biosensors, molecular filtration, drug delivery, and tissue engineering [44–50]. To obtain these applications the crystallization of TiO$_2$ nanotube arrays is required.

2.2 Excimer Laser Crystallization of TiO$_2$

2.2.1 Laser-Solid Interaction

Electromagnetic radiation with wavelength ranging from ultraviolet to infrared interacts exclusively with electrons, as atoms are too heavy to respond significantly to the high frequencies ($v > 10^{13}$ Hz) [51]. Therefore, the optical properties of material are determined by the energy states of its valence electrons. Bond electrons normally weakly respond to the external electromagnetic wave and affect only its phase velocity. However, free electrons can be accelerated and therefore extract energy from the field. Since the field is periodically changing, the oscillating electrons reradiate their kinetic energy or collide with the atoms, giving their energy to the lattice.

Absorption of incident energy fundamentally dictates the resultant thermal state of the material and therefore is a suitable point to begin an analysis of laser-solid interactions. The mechanisms involved in absorption of incident radiation in materials are defined by the electronic structure of the material, and therefore it is useful to discuss exclusively semiconductors. In semiconductors, five distinct mechanisms for the absorption of light can be identified [52].

1) Photons with energy (hv) much less than the band-gap energy (E_g) can excite lattice vibrations directly.

2) Free or nearly free carriers can be excited by absorption of light with $h\nu < E_g$; such carriers will always be present as a result of finite temperature and doping.

3) An induced metallic-like absorption due to free carriers generated by the laser radiation itself can occur.

4) For photon energies are larger than E_g, absorption will take place by direct and indirect (photon-assisted) excitation of electron-hole pairs.

5) Absorption induced by broken symmetry of the crystalline lattice is possible.

When a beam of photons of energy $h\nu > E_g$ is absorbed in a semiconductor, excited carriers, which results in lattice heating [53], is a complicated process and an field of active research [54]. As incident radiation is converted to increasing lattice temperatures, the thermophysical properties of the material dictate temperature distribution and phase changes. This aspect of laser annealing area has been actively investigated [55-59].

2.2.2 Eximer Laser Crystallization of TiO$_2$

The basic mechanism of laser heating proceeds is through photon absorption and the subsequent rapid transfer of energy from the electrons to the lattice [60-62]. During laser annealing a beam of photons is focused on a sample. Simply put, the photons interact with the electrons in the sample which then transfer the energy to the lattice. This causes localized heating in the area where the photons hit the sample. More specifically, the wavelength of this light determines how the energy will be absorbed in the TiO$_2$. The energy of the beam, or incident photon energy, is determined by the equation:

$$E = hc/\lambda$$

with h equal to Planck's constant, c equal to the speed of light, and equal to the wavelength of the laser. With the bandgap of TiO$_2$ around 3 eV, laser energy greater than this bandgap results in absorption via band-to-band transitions, which results in the desired heating of the region. When the heating is sufficient, phase transitions may occur. In order to transform

10

amorphous to anatase TiO_2, it is necessary to overcome an activation energy ($E_{\alpha-A}$) of 137 kJ/mol [64]. In contrast, higher activation energy (E_{A-R}), 350 to 500 kJ/mol [65-66] is required to enable the phase transition from anatase to rutile.

2.3 Applications of ELA for Flexible Substrate Devices, and other Applications

High temperature processing steps such as thermal annealing that are incompatible with plastic substrates are still a major hindrance. Laser annealing permits localized energy input without affecting the underlying substrate and can help overcome this problem.

In semiconductor technology, laser crystallization has been widely used for advantages of selective absorption and low substrate temperature. Moreover, the scanning area can be freely selected without heating other regions. The adoption of this technique can incorporate the fabrication of ferroelectric thin films into large scale integrated circuit processing and make mass production possible. For example, the ferroelectric perovskite phase in $PbZr_{0.44}Ti_{0.56}O_3$ (PZT) films on glass substrates were carried out by using laser annealing [63]. The substrates were kept at room temperature during the whole fabrication process. This work has made the processing of ferroelectric films compatible with Si integrated circuit technology. The other advantage of laser annealing technique is that ferroelectric films with random patterns can be made without heating other parts of a device due to the controllability of the scanning laser spot. In addition, laser annealing at 200° C substrate temperature of $SrTiO_3$ films deposited at 200° C shown the improvement of the crystallinity of the films [67]. Several reports also have been presented on the study of the laser annealing of $Pb(Zr, Ti)O_3$, PZT, $PbTiO_3$ (PT) thin films. The reported data on these materials showed that the thin films could be crystallized at a low temperature [20-24].

In industry, production of low temperature p-Si back plates for LCDs by high power excimer laser annealing was introduced several years ago. Regarding the economy of the

process, one of the major advantages of excimer laser annealing is the opportunity to make use of low cost glass substrates due to the low temperature of the annealing process [68].

Beside two excellent major advantages of selective absorption and low substrate temperature of eximer laser annealing technique, the improvement of electrical properties of materials induced by excimer laser irradiation is presented. Recently, Heng Pan [69] et al demonstrated the excimer laser annealing of metal oxide (ZnO) nanoparticles to improve the electrical properties in producing field effect transistors (FETs). In addition, good dielectric properties of $Pb(Zr, Ti)O_3$, PZT, $PbTiO_3$ (PT) thin films obtained after excimer laser irradiation. The influence of laser treatment on electrical properties of TiO_2 thin films has been reported by J. H. Kim et al [26]. This research showed that the permittivity of TiO_2 films increase with increasing laser powers and the number of laser shots at constant laser power. It can be explained that laser-irradiation of TiO_2 films at room temperature produced oxygen vacancies at the film surface and new Ti valences. The electrons and space charges produced through the defect chemistry increased permittivity in laser-irradiated TiO_2 films. It opens commercially applications of high permittivity TiO_2 films for polymer metal-insulator-semiconductor field-effect transistors (MISFETs).

Chapter 3 Experimental

This chapter will cover the experimental method for TNAs preparation, annealing techniques and characterization of the TNAs. The first section will describe the procedures for preparing the TNAs samples. All samples used in this work were made with two-electrode electrochemical cell consisting of a stainless steel foil (SS304) as the cathode and a Ti foil as the anode, at constant DC potential at 20 V for 24 hours. In addition, annealing systems were introduced for solid phase crystallization and excimer laser crystallization. The following section will explain the techniques used to measure the properties of the TNAs. Various analytic tools were employed to investigate the microstructure, impurities, and morphology of the TNAs. These techniques include X-ray diffraction (XRD), X-ray absorption spectroscopy, Raman spectroscopy, and scanning electron microscopy (SEM).

3.1 Sample Preparation

Titanium foil (99.9% purity, 0.05 cm thick) was used as the substrate for forming TiO_2 nanotubes by anodic oxidation. Prior to anodization, the Ti foil was ultrasonically cleaned with acetone, ethanol, rinsed with distilled water and then dried by purging N_2 gas. All anodization experiments were carried out at room temperature using a two-electrode electrochemical cell consisting of a stainless steel foil (SS304) as the cathode and a Ti foil as the anode, at constant DC potential at 20 V for 24 hours. The electrolyte is a mixture of ethylene glycol, 0.5 wt% NH_4F, and 3 wt% H_2O. Schematic diagram of anodization reaction system is illustrated in Figure 3-1.
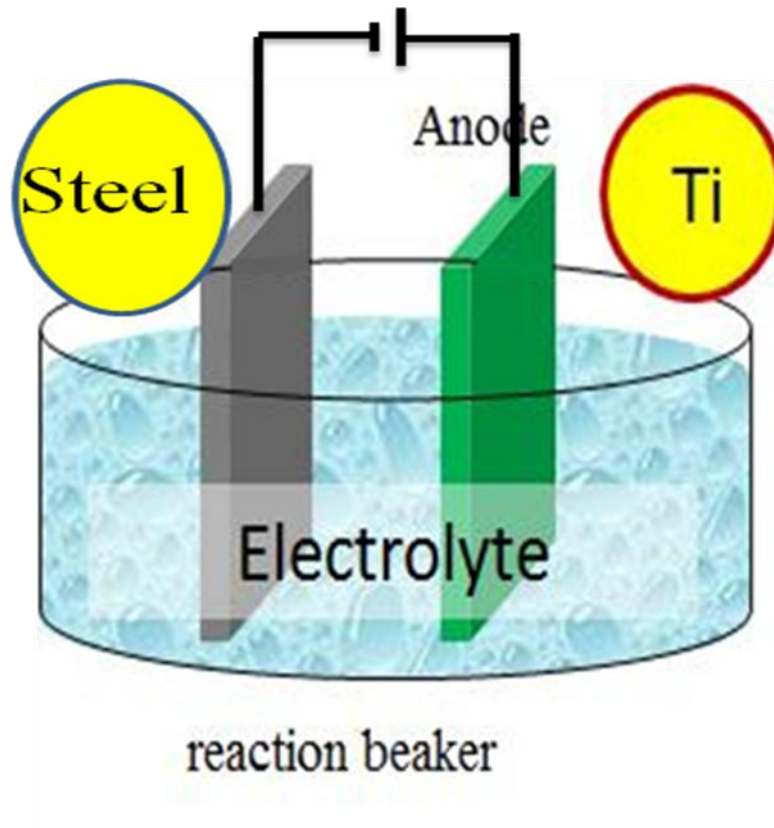
Figure   3-1   Schematic diagram of anodization reaction system
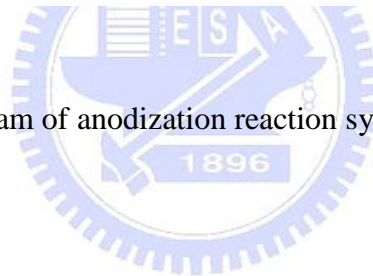
3.2 Film Annealing

3.2.1 Excimer Laser Annealing (ELA) System

Laser annealing was performed with a Lambda Physik Complex 201 excimer laser operating at 248 nm wavelength (KrF) and pulse width ~ 25 ns (FWHM). Energy of source was varied in the laser control system to alter the beam energy and hence energy density on the sample. Frequency of laser was also varied to change the number of pulses per unit time. Duration of laser treatment was measured by timer. Schematic diagrams of the laser setup for experiments are illustrated in Figure 3-2, where the angle between laser beam and sample is α.
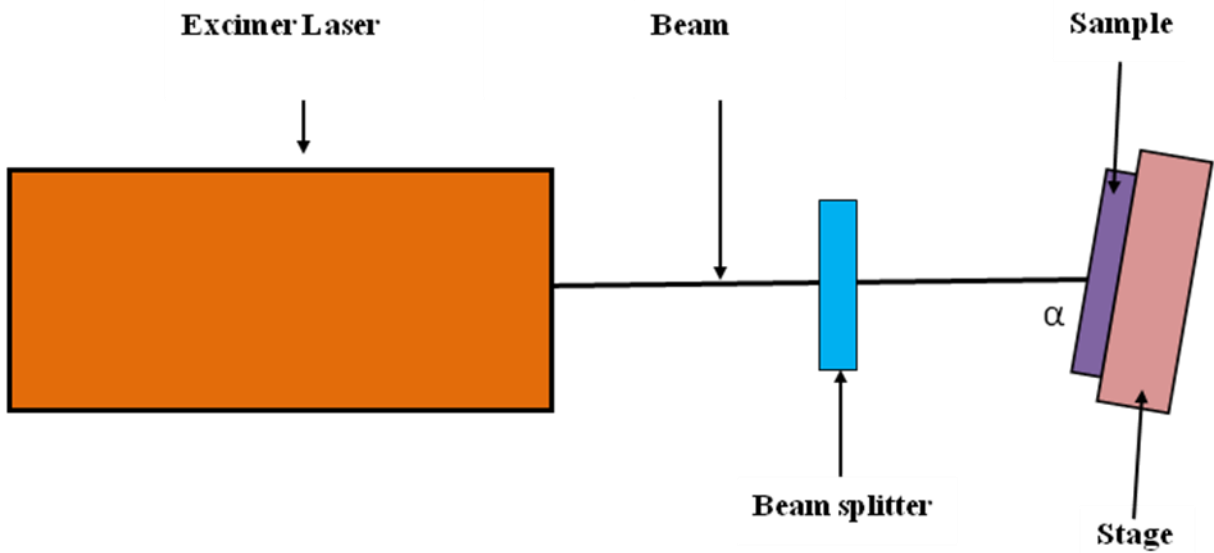
Figure 3-2   Schematic of the experimental setup for laser anneal of TNAs/Ti samples

We designed two modes of experiments: (1) parallel mode and (2) tilted mode. In the parallel mode, the angle α is set equal 90° and the stage is fixed as illustrated in Figure 3-3.
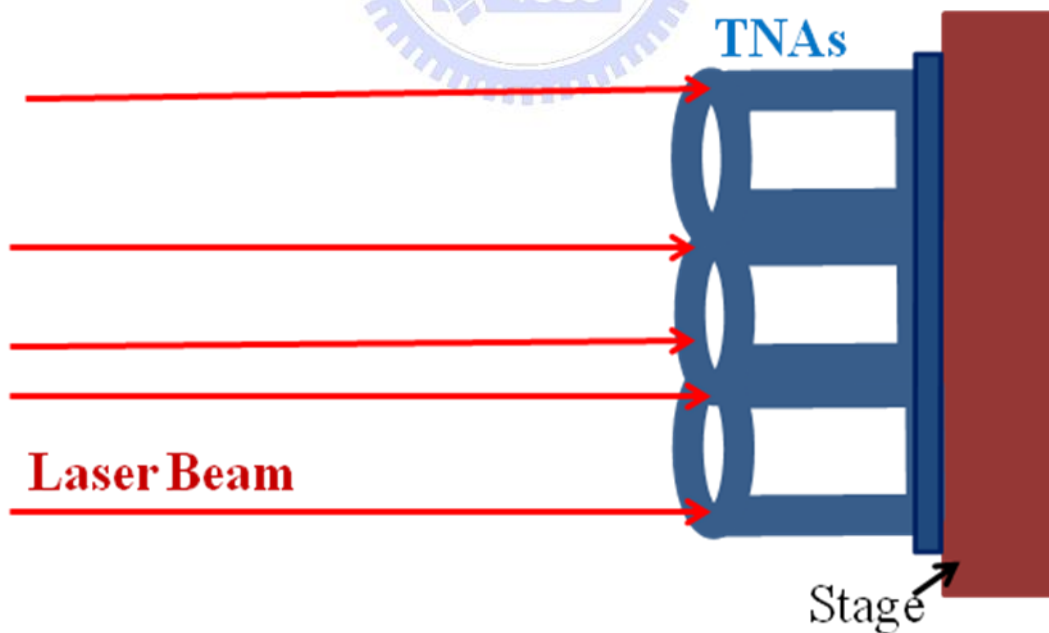
Figure 3-3   Schematic of laser anneal of TNAs/Ti samples in parallel mode

In the tilted mode, as illustrated in Figure 3-4, the angle α between laser beam and sample can vary from 0° to 90°. In addition, sample can turn rotate around an axis d, which is perpendicular to sample plane (stage) with a turning angle θ of ranging from 0 to 360^0 (Figure 3-4 (b)).
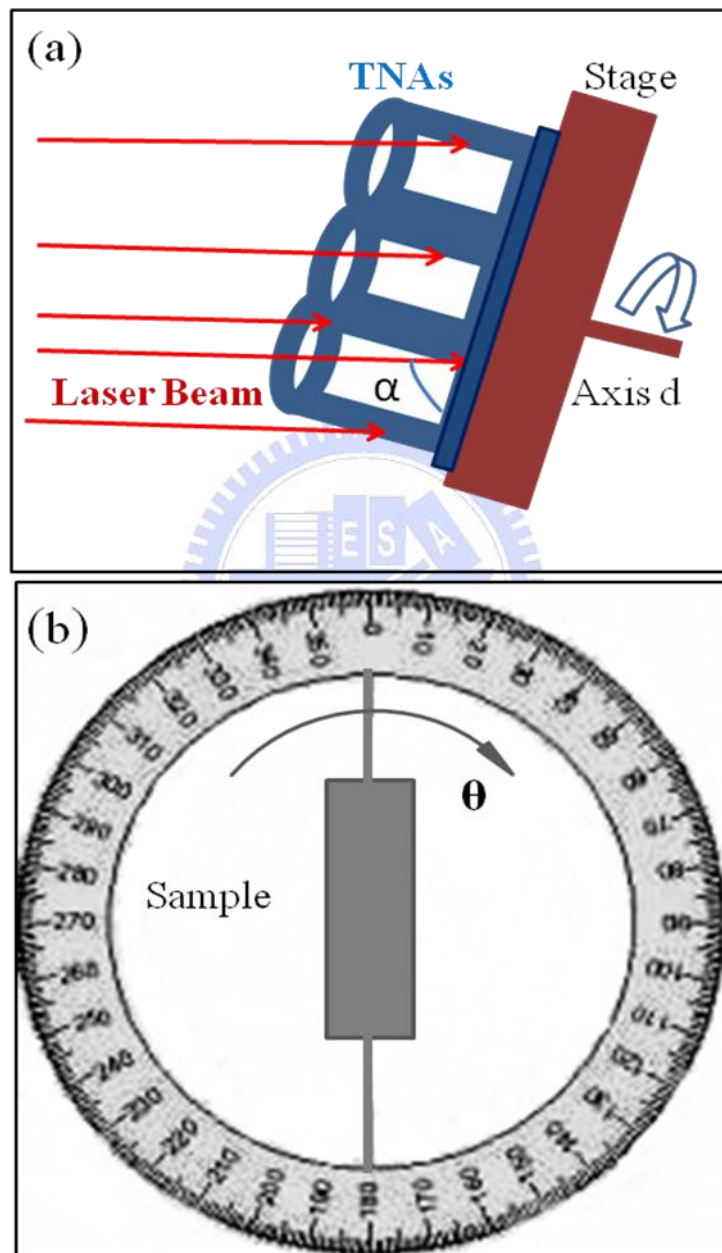
Figure 3-4   Schematic of laser anneal of TNAs/Ti samples: (a) side view and (b) top view in tilted mode

3.2.2. The Post-annealing Treatment of TNAs/Ti by Furnace

The TNAs/Ti samples were annealed in ambient using a conventional furnace. A tungsten wire heater was rolled around the quartz tube to create a homogeneous temperature in the furnace. The schematic of the furnace is shown in Figure 3-5. Moreover, Figure 3-6 shows the diagram of temperature profile for annealing of TNAs/Ti samples in the furnace.
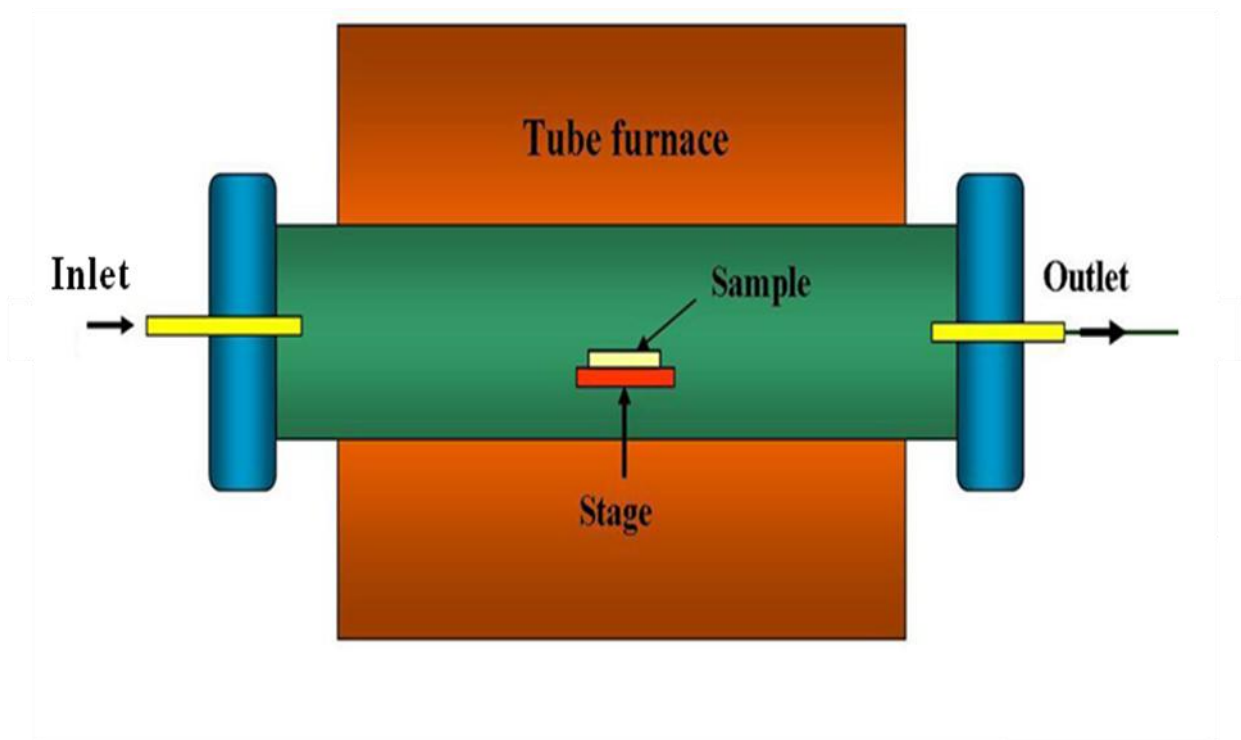
Figure 3-5   Schematic diagram of furnace with 3-zone temperature controllers
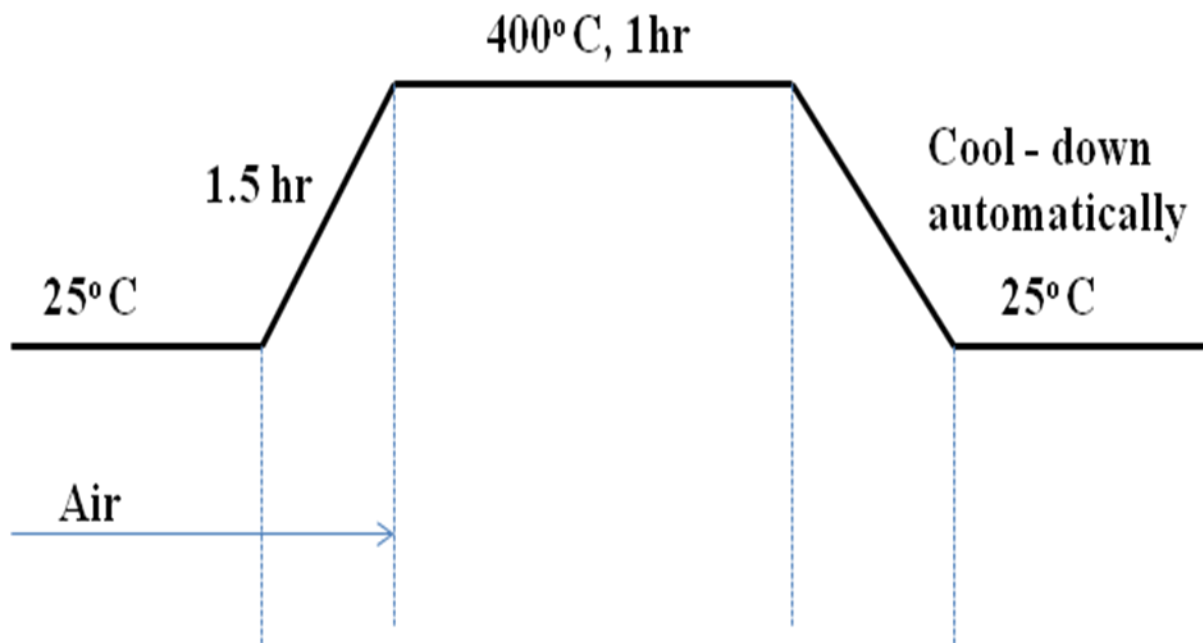
Figure 3-6   Temperature profile in the furnace annealing

3.3 Analytical Techniques

3.3.1 X-ray Diffraction (XRD)

X-ray diffraction (XRD) is a non-destructive tool for analyzing material properties such as crystallinity, the phase identification, and orientation. In addition, grain size and strain can also be easily analyzed with this technique.

XRD was utilized to analyze the crystallinity, the phase identification of TNAs/Ti samples. The samples were scanned by Siemens Diffractometer D5000 (NCTU) with Cu Kα (λ=1.5405Å) source and using synchrotron beamline 17 B1 at National Synchrotron Radiation Research Center in Hsinchu, Taiwan (NSRRC). During scanning period, X-ray beam of wavelength λ was irradiated to the sample at an angle θ, and the diffracted intensity at an angle 2θ was recorded by a detector as illustrated in Figure 3-7. All of scans use θ-2θ mode with 2θ ranging from 20° to 50°.
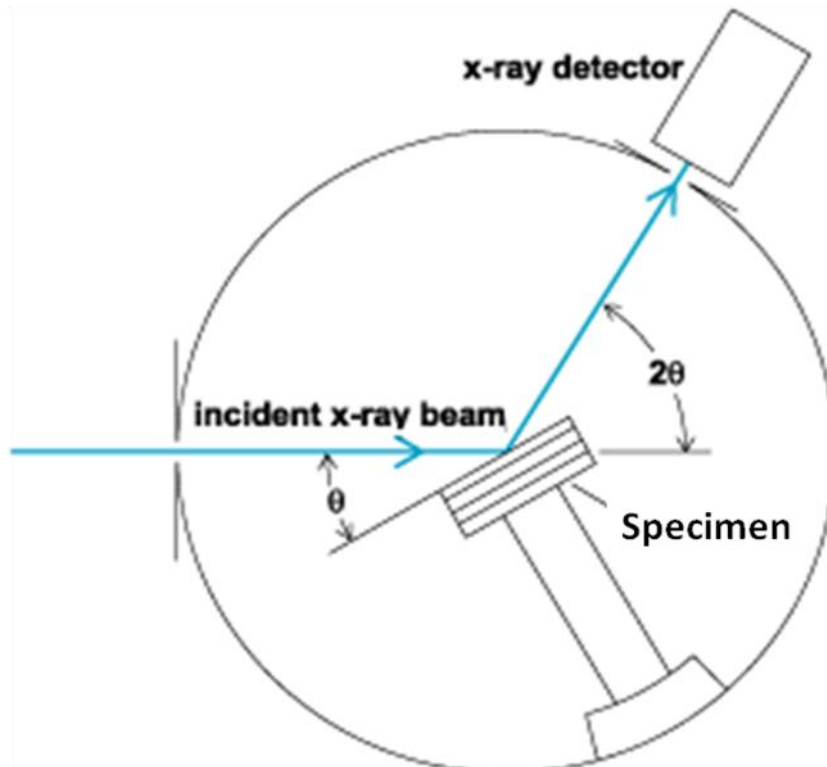
Figure 3-7   Definition of the angle of incidence and diffraction in an XRD experiment

3.3.2 X- ray Absorption

The XANES measurement were performed using the beam line 20 A of National Synchorotron Radiation Research Center (NSRRC), Hsinchu, Taiwan. The XANES spectra were collected in the vicinity of titanium L-edge (445-480 eV) and oxygen K-edge (520-570 eV) regions. All spectra in this thesis were measured in total electron yield mode (TEY) using a high-energy spherical grating monochromoter with energy resolution of about 1/8000 [70], by monitoring the total sample photocurrent as a function of photon energy scanned through Ti $L_{2,3}$-edge. The overall experimental resolution around the Ti $L_{2,3}$ edge was 100 meV. All spectra were collected at room temperature and the chamber pressure was about $2x10^{-8}$ Torr or better. The incoming radiation flux was monitored by the total photocurrent produced in a clean Au mesh inserted in the beam.

During XANES measurement, the incident X-ray beam was irradiated directly to the surface of samples. Moreover, X-ray beam was only absorbed by the surface layer sample. Therefore, the XANES results will describe the characteristics of the surface layer of sample. With the TNAs were annealed by furnace, the heating sample was homogeneously leading to the crystalline structure of sample was uniformly. In this case, the properties in entire sample can be the analyzed basing on XANES results. On the other hand, when the TNAs were irradiated by laser in parallel mode, the surface layer of sample was annealed by laser first and following by internal parts of sample. Hence, the XANES results will only explain the properties of the surface layer of sample annealed by laser.

The incident photo intensity (I_o) was calibrated by aligning the Ti $L_{2,3}$ and O K-edges of a $SrTiO_3$. All the X-ray absorption spectra were then normalized to I_o. To perform the fitting for the amount of crystalline, amorphous phases and impurities in TNAs grown in NH_4F solutions and after using excimer laser annealing with specific conditions, we used the intensity ratios of orbitals in the O K-edge according to the published spectra [71-75] to determine the oxidation states of Ti. The fitting of a mode with various orbitals performed with a program with the Maximum Likelihood (ML) estimator to match spectra for experimental spectra [76]. Then the edges from TiO, Ti_2O_3, TiO_2 (anatase) and TiO_2 (amorphous) were added to the background. The fitting mode comprises a power-law background AF^{-r}, where E is the photon energy, A and r are tow parameters to be estimated the amount of oxidation states, crystalline and amorphous phases [76]. More details about creating a model and its fitting procedure can be found in the literature [76-77].

3.3.3 Raman Spectroscopy

Raman spectroscopy is a spectroscopic technique used in condensed matter physic and chemistry to study vibrational, rotational, and other low-frequency modes in a system. It relies

on inelastic scattering, or Raman scattering, of monochromatic light, usually from a laser in the visible, near infrared, or near ultraviolet range. The laser light interacts with phonons or other excitations in the system resulting in the energy of the laser photons being shifted up or down. The shift in energy gives information about the phonon modes in the system. The Raman Effect occurs when light impinges upon a molecule and interacts with the electron cloud of the bonds of that molecule. The incident photon excites the molecule into a virtual state. For the spontaneous Raman Effect, the molecule will be excited from the ground state to a virtual energy state, and relax into a vibrational excited state, which generates Stokes Raman scattering. If the molecule was already in an elevated vibrational energy state, the Raman scattering is then called anti-Stokes Raman scattering as shown Figure 3-8. A change in the molecule polarization potential or amount of deformation of the electron cloud with respect to the vibrational coordinate is required for the molecule to exhibit the Raman Effect. The amount of the polarizability change will determine the Raman scattering intensity, whereas the Raman shift is equal to the vibrational level that is involved.

In this research Jobin Yvon Horiba Scientific Raman Spectrometer was used. All the Raman spectra were recorded with a double grating spectrometer in backscattering geometry, at room temperature; the He–Ne laser (632.8 nm) was used for the excitation. The diameter of the spot in the sample was typically 1 µm.
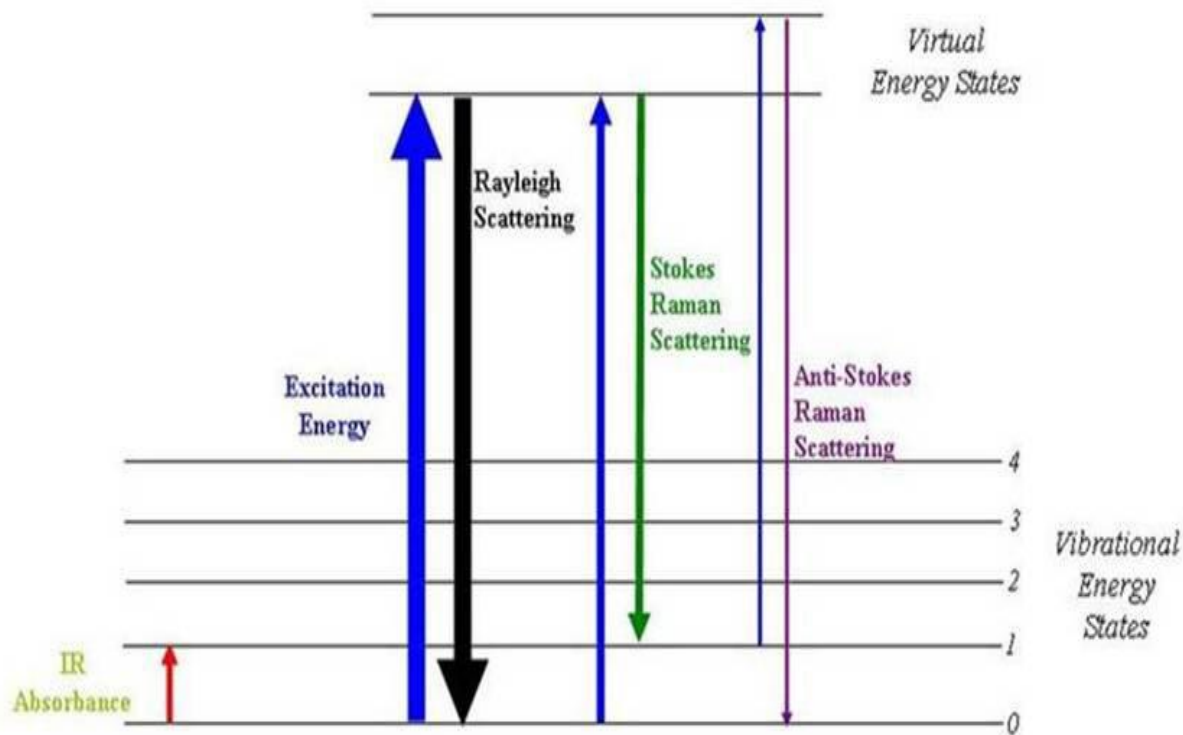
Figure 3-8   Energy level diagrams showing the states involved in Raman signal [78]

3.3.4 Scanning Electron Microscopy (SEM)

Field emission scanning electron microscopy (FESEM) (JEOL 6700F) was employed to examine the surface structure and the cross sectional morphology of the TiO_2 nano-tubes films annealed by the furnace and excimer laser. The JEOL 6700F was operated at 15kV, while the emission current was set at 10 µA and the operating pressure was under 9.6 x10^{-5} Torr.

Chapter 4 Results and Discussion

4.1 Structure of Titania nanotube Arrays (TNAs)

Figure 4-1 illustrates the surface and cross-section morphology of TNAs prepared by anodic oxidation in NH_4F solution. As seen in Figure 4-1 (a) self-organized regular porous TiO_2 structure consists of pore arrays with a uniform pore diameter of approximately 50 nm, wall thickness of 20 nm. TNAs of 7 µm (140:1 aspect ratio) in length were obtained using a high viscosity ethylene glycol electrolyte with 0.5 wt% NH_4F, and 3 wt% H_2O as shown in Figure 4-1 (b). It has been proposed that neutral solutions suppress the chemical dissolution of oxidized TiO_2 in comparison with acidic aqueous solutions like aqueous HF [79-80]. Dimethyl sufoxide and ethanol mixed solutions were found to yield TO_2 nano-tubes with approximately 2 µm length after 70 h anodization [79], displaying a rather low growth rate for neutral non-aqueous electrolytes. In addition, Cai et al [80] reported that TiO_2 nano-tubes of 4.4 µm in length was prepared by adding more H_2SO_4 and citric acids. It clearly showed that both the electrolyte and pH value are critical factors controlling the nano-tube morphology and its growth rate. The key for obtaining high-aspect-ratio growth is to adjust the ionic diffusion coefficient of electrolyte, which was responsible for maintaining a high H^+ concentration at the pore bottom with a protective environment maintained along the pore walls and at the pore walls as well as the pore mouth during chemical drilling [8].
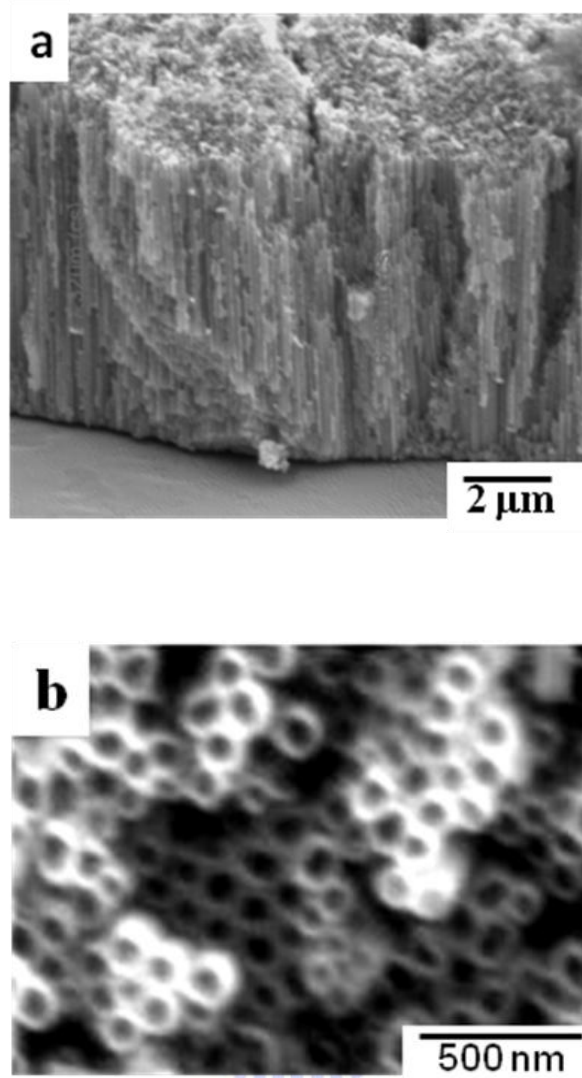
Figure 4-1   FESEM images of TiO$_2$ nanotubes arrays prepared by anodic oxidation in NH$_4$F solution. (a) Cross sectional image and (b) top view image

4.2 The Effect of Excimer Laser Annealing Conditions on Microstructure and Surface Morphology of TNAs

4.2.1 The Effect of Laser Fluence on TNAs

4.2.1.1 The Effect of Laser Fluence on the Crystallization of TNAs

Figure 4-2 shows the XRD spectra of TNAs/Ti samples annealed by laser with various laser fluence values at 9000 shots. As-grown TiO_2 nanotube arrays prepared in NH_4F solution at room temperature are completely amorphous. When TNAs were irradiated by laser with fluence between 0.067 and 0.133 Jcm^{-2}, A (101) and A (200) peaks of anatase (A) appeared and no rutile (R) peak was visible. It implies that the amorphous structure was transformed to polycrystalline anatase after laser irradiation. When fluence range was between 0.133 and 0.4 Jcm^{-2}, anatase peaks became stronger and rutile peaks such as R (110), R (101), and R (111) appeared. Hence, in this case, the ELA process made TNAs transform from amorphous to anatase and then anatase phase continues transforming to rutile. However, intensities of anatase peaks are stronger than rutile peaks, indicating that anatase is still the dominant phase. Moreover, the intensities of anatase peaks as well as rutile peaks increase with the increasing of fluence. It shows that crystallization of samples increases with increasing fluence.
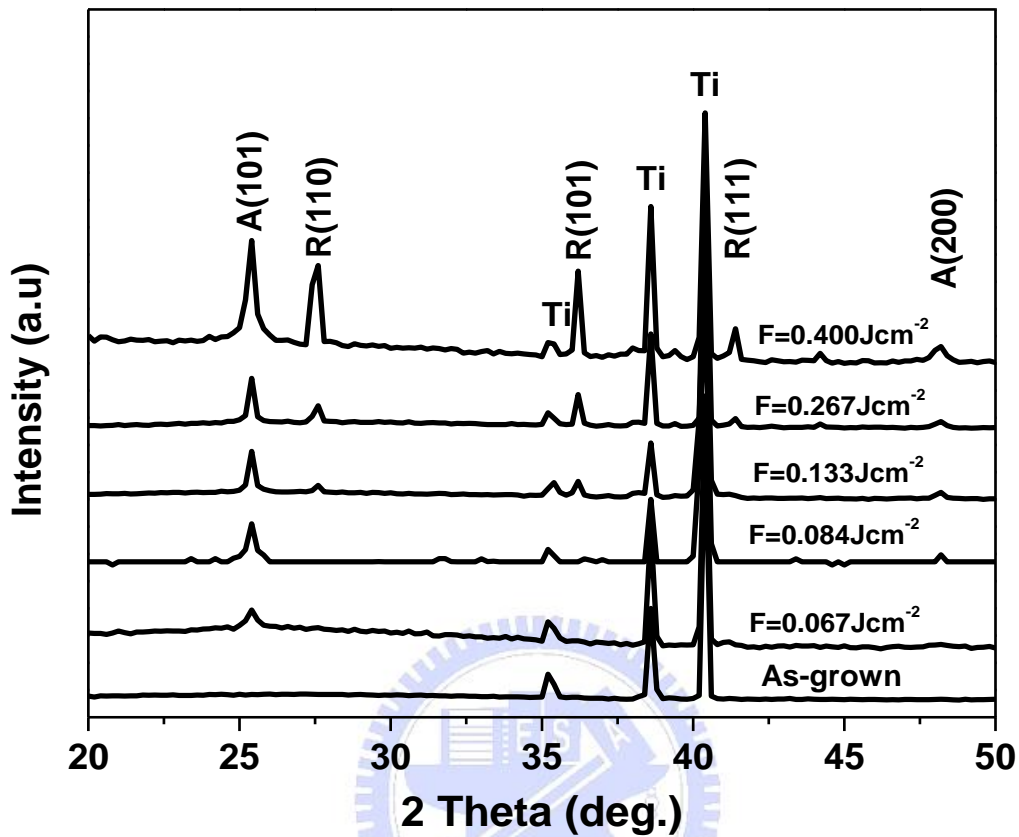
Figure 4-2   XRD spectra of the TNAs/Ti samples annealed by excimer laser with various fluences at 9000 shots

The Raman spectra of as-grown TNAs/Ti samples and annealed by laser with different fluences of 0.084 Jcm^{-2}, 0.133 Jcm^{-2}, and 0.4 Jcm^{-2} at 9000 shots are illustrated in Figure 4-3. The vibrational bands corresponding to the four active fundamental modes of anatase are recorded at 397 cm^{-1} (B_{1g}), 518 cm^{-1} (A_{1g} and B_{1g} unresolved) and 640 cm^{-1} (E_g). No Raman peak is observed in the case of the as-grown sample. Evidence of a crystalline phase started to show after laser irradiation at fluence of 0.084 Jcm^{-2}. Further increase of laser fluence to 0.133 Jcm^{-2}, the anatase active fundamental modes became stronger and two rutile's Raman active modes also appeared at 448 cm^{-1} (E_g) and 613 cm^{-1} (A_{1g}). It shows more clearly in the case of sample annealed by laser with fluence of 0.4 Jcm^{-2}, all of the Raman active modes of

anatase and rutile become higher. It implies that the amorphous phase was continuously transformed to crystalline phases when fluence increased from 0.133 Jcm^{-2} to 0.4 Jcm^{-2}. Therefore, we can conclude that the TNAs annealed by laser with fluence of 0.133Jcm^{-2} or below 9000 shots still remain amorphous phase.
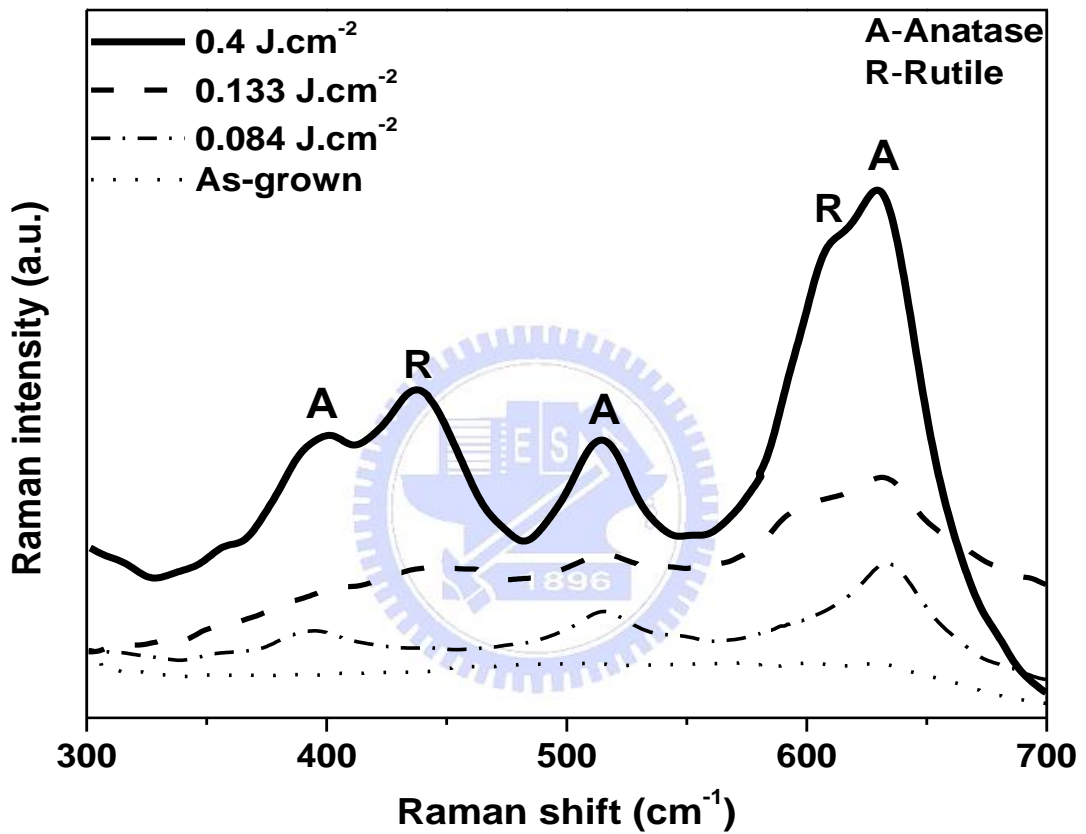
Figure 4-3   Raman spectra of TNAs/Ti samples as-grown and annealed by laser with
various fluences at 9000 shots (Raman laser radiation: 632.8 nm)

XRD and Raman results indicate that TNAs irradiated by laser with fluence is less than 0.133 Jcm^{-2} at 9000 shots contain anatase and amorphous phases, while fluence is higher than 0. 133 Jcm^{-2}, TNAs possess all of amorphous, anatase and rutile phases.

4.2.1.2 The Effect of Laser Fluence on Surface Morphology of TNAs

　　Figure 4-4 shows the surface morphology and cross sectional images of TNAs annealed by laser with various laser fluences at 9000 shots. When TNAs irradiated by laser with fluence are less than 0.133 Jcm^{-2}, almost no damage is observed as shown in Figures 4-4 (a) and (b). In contrast, with fluence higher than 0.133 Jcm^{-2} (Figures 4-4 (c-e)), the surface morphology of TNAs appears to be strongly modified. The cross sectional images of TNAs show that the damage of tubes appeared only on the top of tubes. Since the laser beam is irradiated directly to the top of TNAs in parallel mode, the laser energy is transferred from the top to bottom of tubes, leading to the surface of TNAs received larger energy and was damaged.
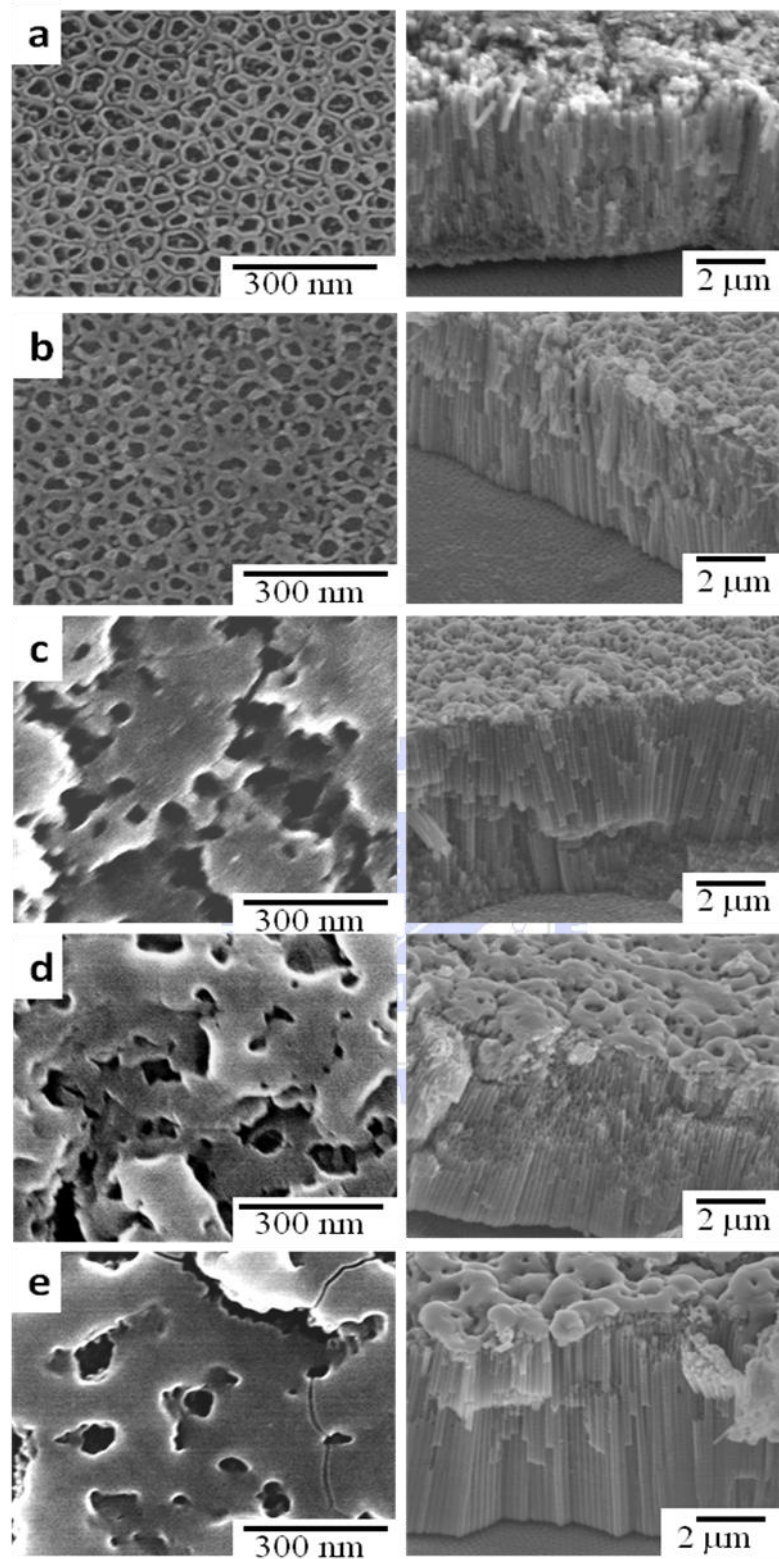
Figure 4-4   Surface morphology and cross sectional images of TNAs annealed by laser with different fluences: (a) 0.067 Jcm^{-2}, (b) 0.084 Jcm^{-2}, (c) 0.133 Jcm^{-2}, (d) 0.267 Jcm^{-2}, and (e) 0.4 Jcm^{-2} at 9000 shots

4.2.2 The Effect of the Number of Laser Pulses (shots) on TNAs

4.2.2.1 The Effect of the Number of shots on the Crystallization of TNAs

Figure 4-5 presents XRD spectra of the TNAs/Ti samples annealed by laser with fluence at 0.1 Jcm^{-2} and different shots from 3000, 9000 to 18000. The anatase peaks appear in XRD spectra of the TNAs/Ti samples annealed by laser with 3000 or 9000 shots, and no rutile peaks is observed. It shows that TNAs amorphous is transformed to anatase under these laser annealing conditions. However, when the shot number is increased to 18000, the rutile peaks are visible along with the dominant anatase peaks. It suggests that laser anneal of TNAs/Ti samples with shots higher than 9000 result in transformation of amorphous phase to anatase and rutile phases. A comparison of TNAs irradiated by 3000 and 9000 shots revealed that the peak height of anatase A (101), *i.e.* amount of anatase increases with increasing shot number.
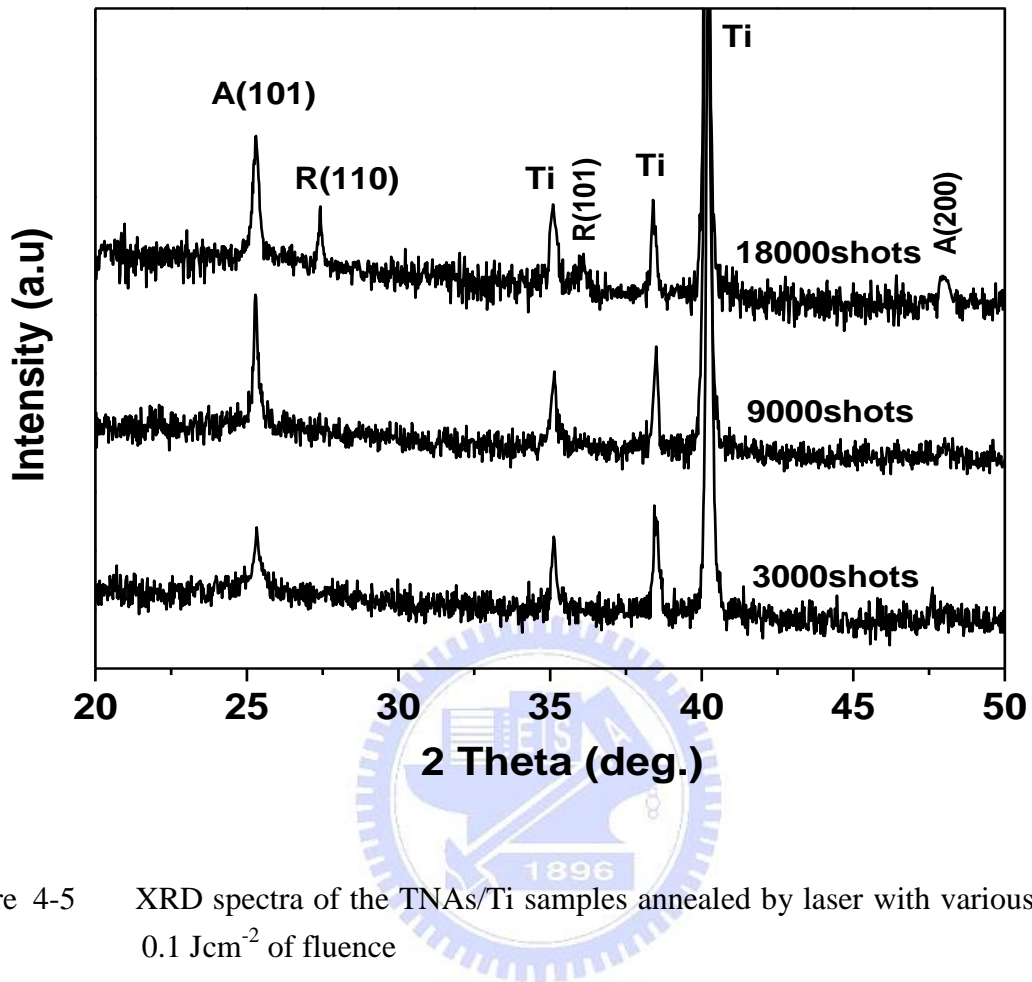
Figure 4-5   XRD spectra of the TNAs/Ti samples annealed by laser with various shots at
              0.1 Jcm^{-2} of fluence

4.2.2.2 The Effect of the Number of shots on the Surface Morphology of TNAs

Figure 4-6 shows the surface morphology and cross sectional images of TNAs irradiated by laser with different shots from 3000, 9000 to 18000 at fluence of 0.1 Jcm^{-2}. As seen in Figure 4-6(a), TNAs irradiated by laser with 3000 shots, few tubes are destroyed. However, as the shot number is increased to 9000 or 18000 shown in Figure 4-6 (b) and (c), the broken tubes increase and combine together. As a result, the melting layer is formed on the top of nanotube arrays. The damage of TNAs surface increases with increasing number of shots.

31
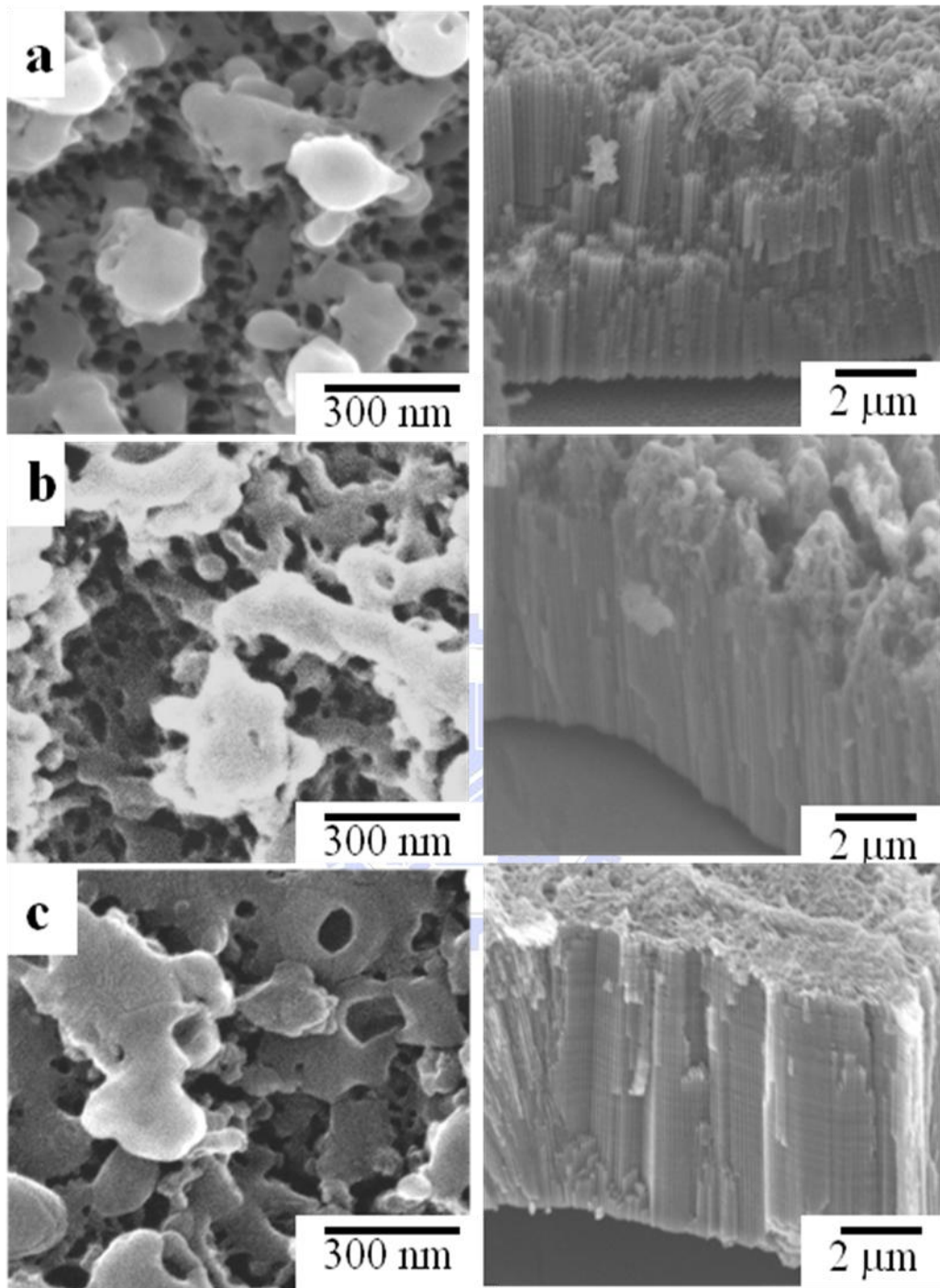
Figure 4-6   Surface morphology and cross sectional images of TNAs annealed by laser

with (a) 3000 shots, (b) 9000 shots, and (c) 18000 shots at 0.1 Jcm^{-2} of fluence

4.3 Quantitative Analysis of TNAs Multi-phase Structure based on XRD Results

The phase composition of TNAs calculated basing on quantitative analysis of XRD results. Quantitative analysis of diffraction data usually refers to the determination of amounts of different phases in multi-phase samples. In this paper, an effort is made to determine structural characteristics and phase proportions with quantifiable numerical accurateness from the experimental data. New X-ray diffraction method for quantitative mixture structure analysis, for example, matrix flushing method has been developed. This is much simpler and faster than, yet as reliable as, the conventional internal-standard method [81] because the matrix flushing theory gives a precise relationship between intensity and concentration free from matrix effect. The analytical procedures are described briefly below.

For specimen containing many components, such as *1, 2*, etc., a simple relationship between intensity and concentration free from matrix effect, can be expressed by Eq. (1)

$$\frac{I_1}{I_2} = \alpha \frac{\chi_1}{\chi_2} \qquad (1) \qquad \text{with} \qquad \alpha = \frac{k_1}{k_2}$$

Where:

I_1 is intensity of X-rays diffracted by a selected plane (hkl) of component *1*;

χ_1 is weight fraction of component *1*; k_1 is a constant which depends upon the geometry of diffractometer and the nature of component *1*.

Similarly, I_2, χ_2, and k_2 parameters are corresponding to component *2*.

For comparison and calculation reference, conventional annealing of TNAs/Ti sample was carried out by a furnace at 400°C for 1 hr. Anatase phase was obtained for W_{A_1} = 86 % of weight (see XANES results). For this sample with two components anatase (A$_1$) and Ti, the relationship can be described by Equation (2) based on Equation (1):

$$\frac{I_{A_1}}{I_{Ti}} = \alpha \frac{\chi_{A_1}}{\chi_{Ti}} \qquad (2)$$

XRD and SEM results show that all of TNAs/Ti samples irradiated by laser will contain anatase phase (A_j). Similar to equation (2) for these samples:

$$\frac{I_{A_j}}{I_{Ti}} = \alpha \frac{\chi_{A_j}}{\chi_{Ti}} \tag{3}$$

Combining Equation (2) with Equation (3):

$$\frac{I_{A_j}}{I_{A_1}} = \frac{\chi_{A_j}}{\chi_{A_1}} = \frac{m_{A_j}}{m_{A_1}} = \frac{W_{A_j}}{W_{A_1}}$$

This leads to

$$W_{A_j} = \frac{I_{A_j}}{I_{A_1}} W_{A_1} \tag{4}$$

Where W_{A_j} is the weight percentage of anatase in the samples j.

For the case of samples including anatase and rutile components, the weight percentage of rutile, W_{R_j}, is calculated through W_{A_j} as following:

$$\frac{I_R}{I_A} = \alpha_{AR} \frac{\chi_R}{\chi_A} = \alpha_{AR} \frac{m_R}{m_A} \qquad \text{leads to} \qquad \frac{I_R}{I_A} = \alpha_{AR} \frac{\sigma_R}{\sigma_A} \frac{W_{R_j}}{W_{A_j}}$$

where m_A and m_R are the masses of anatase and rutile, respectively.

This leads to

$$W_{R_j} = \frac{1}{\alpha_{AR}} \frac{\sigma_A}{\sigma_R} \frac{I_R}{I_A} W_{A_j}$$

or finally

$$W_{R_j} = 1.14 \frac{I_R}{I_A} W_{A_j} \tag{5}$$

where α_{AR} is 0.8 from literature [82], and σ is the density of TiO_2 with $\sigma_A = 3.89$ g.cm^{-3} for anatase and $\sigma_R = 4.26$ g.cm^{-3} for rutile [34, 35].

Figure 4-7 shows XRD spectra of the TNAs/Ti samples annealed by furnace and laser with different conditions. Accurate values of anatase and rutile peaks can be obtained from their respective XRD spectra.
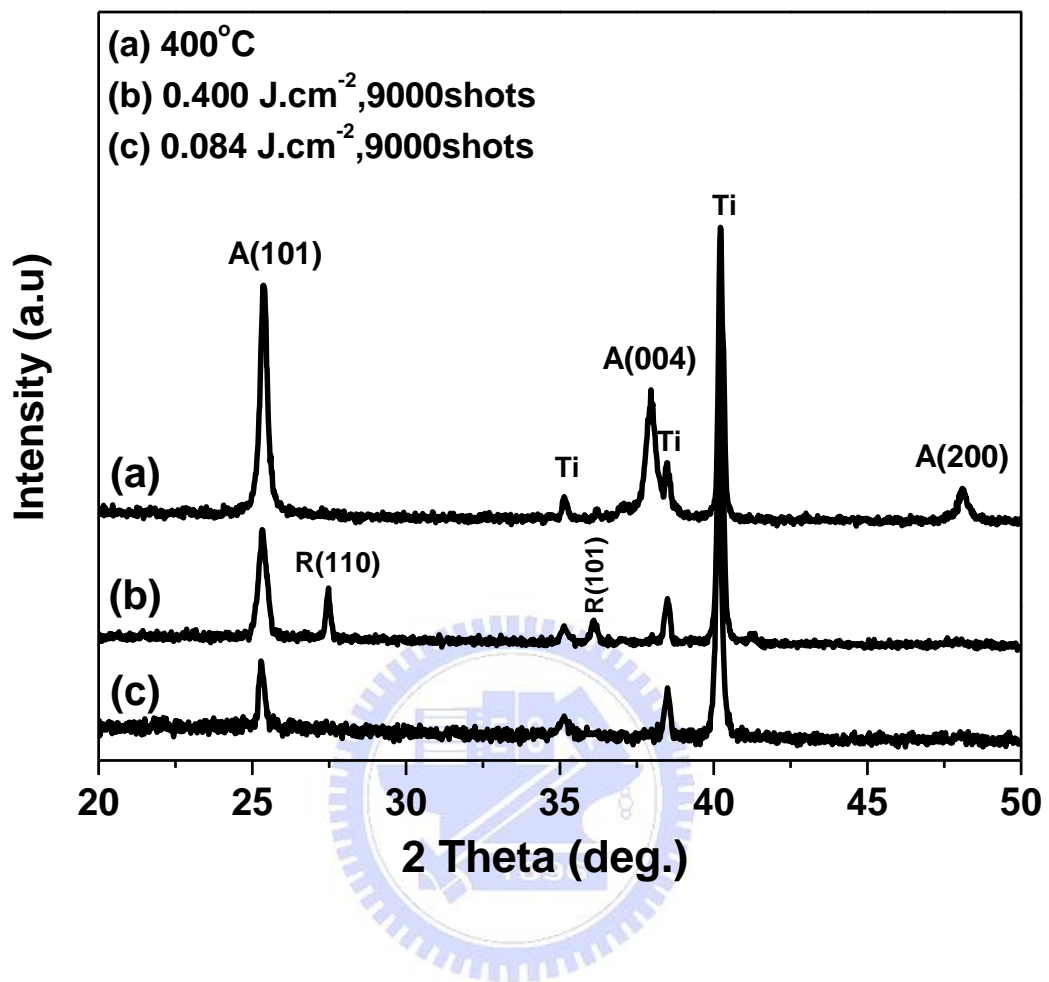
Figure 4-7   XRD spectra of the TNAs/Ti samples annealed by the furnace and by laser
                with different conditions

From XRD results (Figure 4-5 and Figure 4-7) and Equations (4) and (5), the anatase
and rutile peaks intensities and weight percentage of anatase, rutile in the samples annealed by
furnace and laser are summarized in the Table 4-1 below.

Table 4-1   The anatase, rutile X-Ray peaks intensities and weight percentage of anatase,

rutile in samples annealed by furnace and laser. A: anatase, R: rutile

Annealing conditions		Peaks intensities		Weight percentage (%)	
		I_A	I_R	A	R
400^0 C, 1 hr		243	----	86	-----
Various fluences at 9000 shots	0.084	86.9	----	30.75	----
	0.100	87.9	----	31.20	----
	0.400	125.0	68	42.24	26.20
Various shots at 0.1 Jcm^{-2}	3000	59.9	----	21.20	----
	9000	87.9	----	31.20	----
	18000	88.6	58	31.40	20.56

From above results, we conclude that 0.1 Jcm^{-2} of fluence and 9000 shots should be the optimal ELA condition for achieving polycrystalline anatase phase with the high weight percentage. On the other hand, when fluence is higher than 0.133 Jcm^{-2} or shots is over 9000, ELA of TNAs results in multi-phase structure containing both of polycrystalline anatase and rutile. Moreover, weight percentage of anatase and rutile get higher with increasing fluence or shots.

4.4 The Transformation of Impurities TiO, Ti_2O_3 in TNAs to TiO_2 induced by ELA

4.4. 1 XRD Results

Figure 4-8 shows the XRD spectra of TNAs/Ti samples annealed by laser with two laser fluences of 0.042 and 0.1 Jcm^{-2} at 9000 shots. TNAs irradiated by laser with fluence of 0.042 Jcm^{-2}, week anatase (A) A(101) peak is forming. Therefore, the amorphous structure

started transforming to polycrystalline anatase after laser irradiation at 0.042 Jcm^{-2} of fluence. When fluence increase to 0.1 Jcm^{-2}, the intensities of anatase (A) A(101) and A(200) peaks rise sharply but no rutile (R) peak is visible. It indicates that the amorphous structure was strongly transformed to polycrystalline anatase under laser irradiation at 0.1 Jcm^{-2} of fluence.
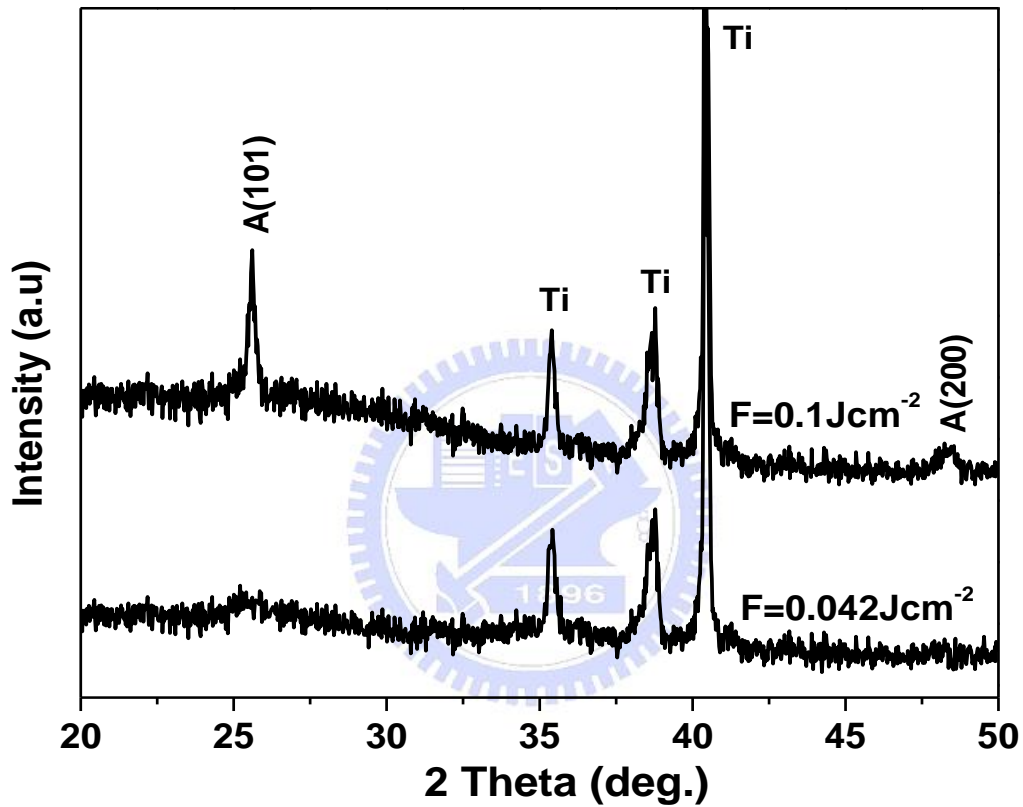
4.4.2 XANES Results

During XANES measurement, the incident X-ray beam was irradiated directly to the surface of samples. Moreover, X-ray beam was only absorbed by the surface layer sample. Therefore, the XANES results describe the characteristics of the surface layer of sample. When the TNAs were irradiated by laser in parallel mode, the surface layer of sample was annealed by laser first and following by internal parts of sample. Hence, the XANES results will only explain the properties of the surface layer of sample annealed by laser.

Ti $L_{2,3}$ edge XANES spectra of TiO_2 nanotube arrays prepared by anodic oxidation in NH_4F solution, subsequently annealed by excimer laser at different fluences of 0.042 Jcm^{-2} and 0.1 Jcm^{-2} at 9000 shots are shown in Figure 4-9. As seen in Figure 4-9, there are four dominant features, which can be attributed to excitations of Ti $2p_{3/2}$ (L_3 edge) and Ti $2p_{1/2}$ (L_2 edge) core levels into empty Ti 3d states. For TiO_2 nano-tube arrays as-grown in NH_4F solution at room temperature, the $L_{2,3}$-edge shows broad features with low intensities in t_{2g} and structureless e_g, which are indicative of amorphous TiO_2 [83]. When as- grown TiO_2 was annealed by laser, the spectra instead show definite crystalline structures as indicated by the sharpness and higher t_{2g} orbitals and double features of e_g orbitals in L_3 edge. Moreover, the leading edge of TNAs annealed by laser also has shifted to higher energy (0.6 eV). It indicates that Ti has changes from lower charge state Ti^0, Ti^{+2}, Ti^{+3} to Ti^{4+} (TiO_2) [84, 85]. This suggested that TNAs prepared at room temperature contain not only amorphous TiO_2 but also some impurities such as TiO, Ti_2O_3 and after annealing by laser, the impurities TiO, Ti_2O_3 were transferred to TiO_2, thus causing the Ti L-edge shift to higher energy.

Figure 4-9   Ti $L_{2,3}$ edge XANES spectra of TiO_2 nanotube arrays prepared by anodic oxidation in NH_4F solution: as-grown, and annealed by laser at different fluences of 0.042 Jcm^{-2} and 0.1 Jcm^{-2} at 9000 shots

Table 4-2 summarizes the intensity ratios of orbitals for Ti L_3 edge of TNAs prepares by anodic oxidation as grown in NH_4F solution, subsequently annealed by laser at different fluences of 0.042 Jcm^{-2} and 0.1 Jcm^{-2} at 9000 shots

Table 4-2   Intensity ratios of the orbitals for Ti L_3 edge of TNAs prepares by anodic oxidation as grown in NH_4F solution, followed by laser annealing with fluences of 0.042 Jcm^{-2}, and 0.1 Jcm^{-2} at 9000 shots

Samples	$I(t_{2g})/ I(e_g)$	$I(b_1)/ I(b_2)$
As-grown	0.90	----
ELA (F=0.042 $J.cm^{-2}$, 9000 shots)	1.02	1.05
ELA (F=0.100 $J.cm^{-2}$, 9000 shots)	1.04	1.04
TiO_2 (anatase)	0.93	1.21
TiO_2 (rutile)	1.20	0.89

As seen in Figure 4-9 and Table 4-2, for all TiO_2 polymorphs, the intensity ratio of $I(L_3\text{-}t_{2g})/ I(L_3\text{-}e_g)$ increases from 0.9 for as-grown sample, to 1.02 and 1.04 as samples annealed by laser at 0.042 and 0.1 $J.cm^{-2}$ of fluence, respectively. Because the intensity of the L-edge features varies with the density of empty d-states, an increase of $I(L_3\text{-}t_{2g})/ I(L_3\text{-}e_g)$ intensity ratio implies an empty state in t_{2g} orbitals, which is consistent with an increase in Ti^{4+} cations. The e_g related peak of the L_3 edge is split into two peaks at 461 eV as the fluence of 0.042 $J.cm^{-2}$ and above. This shows that the major difference between Ti $L_{2,3}$ spectra of amorphous and crystalline phases of TiO_2 is significant change in positions, intensities and widths of e_g-related peak b_1 and b_2. For example, with anatase peak b_1 is substantially stronger than that of peak b_2; while with rutile, the intensity of peak b_2 is substantially stronger than that of peak b_1. In addition, when the fluences is increased from 0.042 to 0.1 $J.cm^{-2}$, the $I(b_1)/ I(b_2)$ intensity ratio is increased 1.04 and 1.05. It means that TNAs annealed by laser with increasing fluence, TNAs are transferred to TiO_2 anatase [86].

Oxygen 1s (K-edge) absorption edges, which consist of the excitation of an oxygen 1s electron into unoccupied 2p-states, are employed to map out the oxygen 2p-projectd density of unoccupied states in order to examine the oxidation states and crystalline phases of TNAs. The O K-edgeXANES spectra of TiO_2 nanotube arrays prepared by anodic oxidation in NH_4F solution: As-grown, and annealed by excimer laser at different fluences of 0.042 Jcm^{-2} and 0.1 Jcm^{-2} at 9000 shots as shown in Figure 4-10.

In general, there are two dominant features in lower energy, 530-536 eV in the O K-edge spectra, which can be assigned to the transitions into Ti 3d t_{2g} and e_g levels. Broad peaks are observed for as-grown TNAs due to slight variation in bond lengths and angles, in hearent to spectra of amorphous TiO_2 solid [82]. However, after annealing by laser at different fluences of 0.042 Jcm^{-2} and 0.1 Jcm^{-2}, the Ti 3d t_{2g} and e_g features become more distinct and narrow shapes of Ti and new peak at higher energy (539.3 eV), which can be attributed to transitions into 4sp orbitals, indicative of anatase phase TiO_2 [85]. In addition, it is interesting to note that the energy separation of both t_{2g} and e_g orbitals provides a direct measure of ligand-field splitting (LFS) of TiO_2. The LFS can be obtained from the corresponding oxygen k-edge spectra, revealing a decrease in sequence of TiO_2 (2.6-2.7 eV), Ti_2O_3 (2.2 eV), and TiO (1.5 eV) [87, 88]. The spectrum of as-grown sample reveals a ligand-field splitting of 2.2 eV. Upon annealing by laser at fluences of 0.042 Jcm^{-2} and 0.1 Jcm^{-2}, LFS increases to 2.6 eV. It indicates that the lower LFS for as-grown sample is due to remaining charge transfer to Ti^{4+}. On the other words, as-grown sample still contain some impurities and annealing by laser there is a charge transfer from Ti^{+2}, Ti^{+3} to Ti^{4+} (TiO_2).
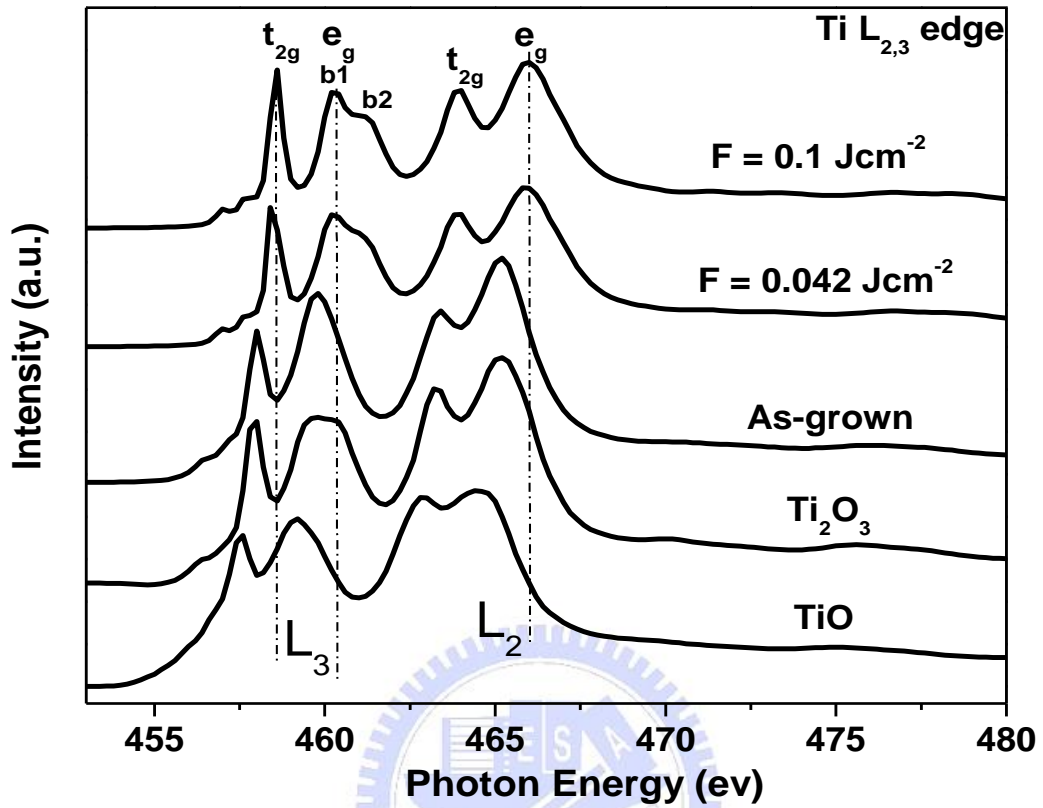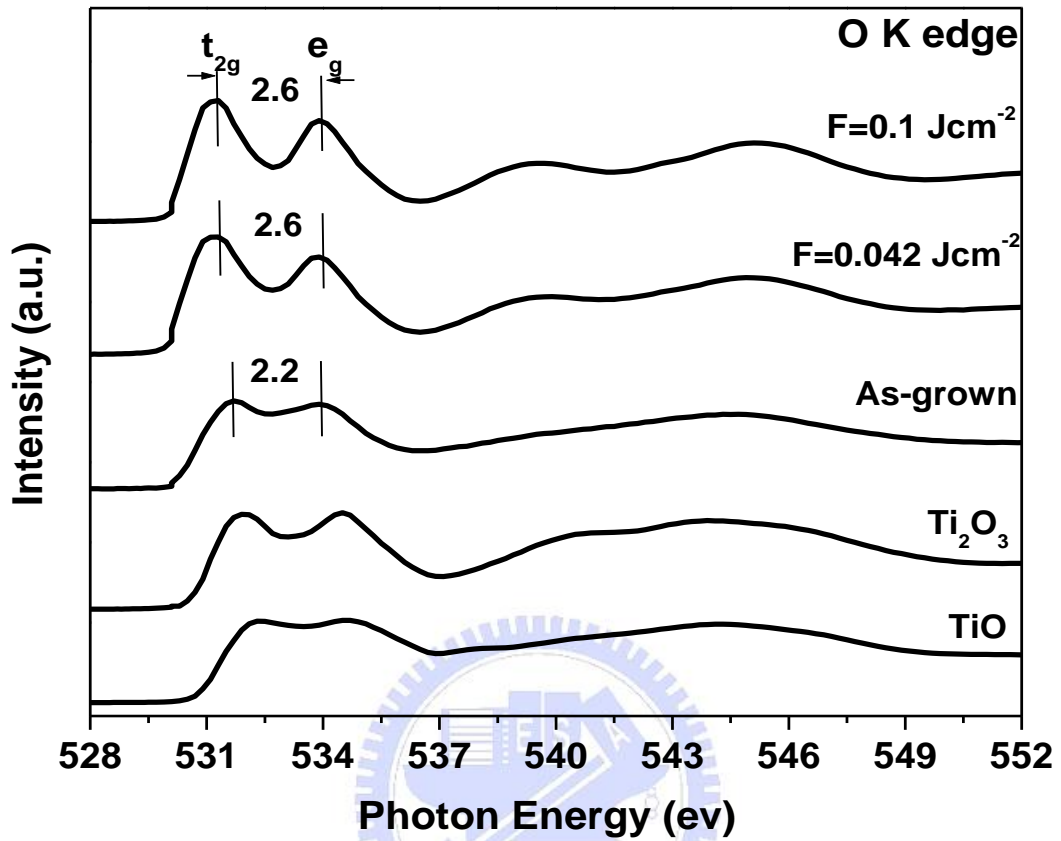
Figure 4-10   O K-edgeXANES spectra of TiO₂ nanotube arrays prepared by anodic oxidation in NH₄F solution: as-grown and annealed by by laser at different fluences of 0.042 Jcm⁻² and 0.1 Jcm⁻² at 9000 shots

Figure 4-11 shows the fitting results for O K-edge XANES spectrum of as-grown TNAs by anodic oxidation in NH4F solution. As seen in the Figure 4-11, the spectra shows that as-grown TNAs at room temperature processes 82 % TiO_2 amorphous phase, 11 % Ti_2O_3, and 7 % TiO. The low percentage of amorphous TNAs prepared in NH₄F solution can be attributed to low oxygen ion formation from only 3 wt% H_2O addition. After that, the TNAs annealed by laser at fluences of 0.042 J.cm⁻² and 0.1 J.cm⁻² or post- annealed at 400ºC.

Figures 4-12 and 4-13 show the fitting results for O K-edge XANES spectra of TNAs annealed by laser at fluences of 0.042 J.cm^{-2} and 0.1 J.cm^{-2}, respectively. As seen in Figure 4-12, the phase transformation has taken place from amorphous to anatase phase (81 %), and particularly all of cations 11 % Ti^{3+} (Ti$_2$O$_3$), and 7 % Ti^{2+} (TiO) are transferred completely to Ti^{4+} (TiO$_2$) after laser treatment at 0.042 J.cm^{-2} of fluence. Further increase of fluence to 0.1 J.cm^{-2}, the percentage of crystallinity for anatase rose to 90 % (see Figures 4-13). Therefore, the increase in fluence from 0.042 J.cm^{-2} to 0.1 J.cm^{-2}, the percentage of crystallinity of TNAs has increased from 80 % to 90 % for anatase phase. On the other hand, the fitting results for O K-edge XANES spectrum of TNAs post-annealed at 400°C (Figures 4-14) shows that 4% Ti$_2$O$_3$ impurity still exists in sample after post annealing. Furthermore, the percentage of TiO$_2$ anatase phase was limited to 86%.

Table 4-3 summarizes the amount of crystalline, amorphous phase and impurities of TiO$_2$ nanotube arrays as-grown, after laser annealing with 0.042 J.cm^{-2} and 0.1 J.cm^{-2} at 9000 shots, and post annealing at 400°C. First, in the as-grown TiO$_2$ nanotube arrays prepared in NH$_4$F solution with low H$_2$O content, at room temperature there is 18 % impurities (11 % Ti^{3+} (Ti$_2$O$_3$), and 7 % Ti^{2+} (TiO) cations) and 82 % amorphous. As the annealing temperature is increased to 400°C, this additional energy enable phase transformation from amorphous phase to anatase phase (86%), and also reduced the impurities from 18% to 4% by charge transferred for Ti cations. However, in the part of TNAs irradiated by laser at 0.042 J.cm^{-2} of fluence, there is not only the phase transformation happened from amorphous to anatase phase, but also all of impurities TiO and Ti$_2$O$_3$ were transferred to TiO$_2$. In addition, further increase of fluence to 0.1 J.cm^{-2}, the crystallinity of TiO$_2$ nanotube has increased to 90% for anatase phase. The above results prove that ELA is powerful technique to make charge transferred for Ti cations from lower charge state Ti^{+2} or Ti^{+3} to Ti^{4+} as well as improve the crystalinity of amorphous TiO$_2$.
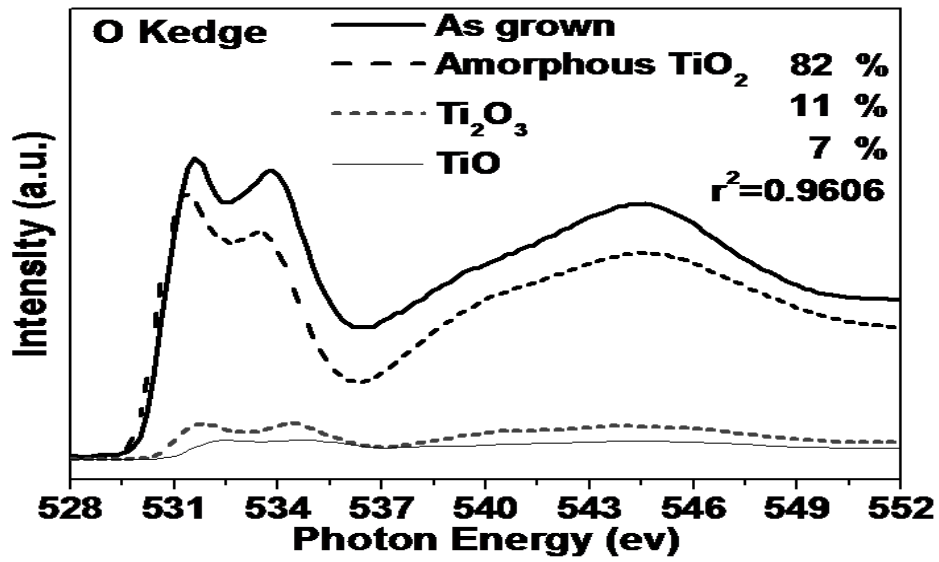
Figure 4-11   Fitting results for O K-edge XANES spectrum of as-grown TNAs
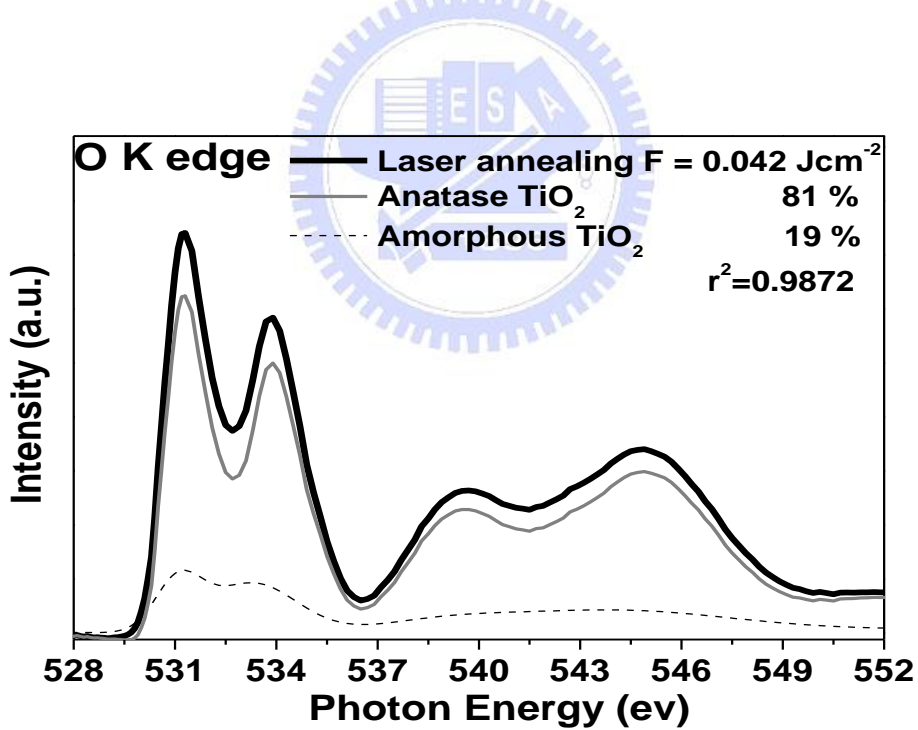
Figure 4-12   Fitting results for O K-edge XANES spectrum of TNAs annealed by laser
with fluence of 0.042 Jcm^{-2} at 9000 shots
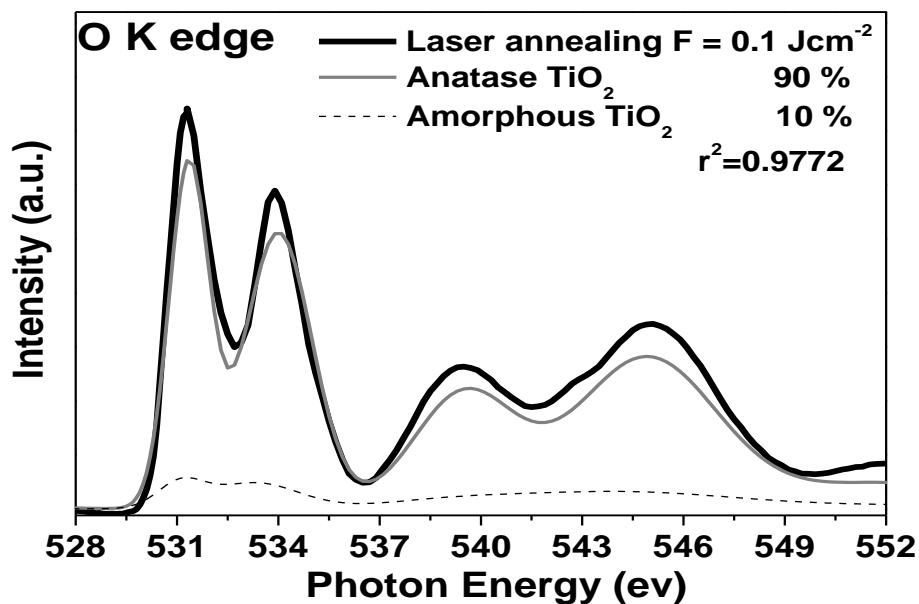
Figure 4-13   Fitting results for O K-edge XANES spectrum of TNAs annealed by laser
with fluence of 0.1 Jcm^{-2} at 9000 shots
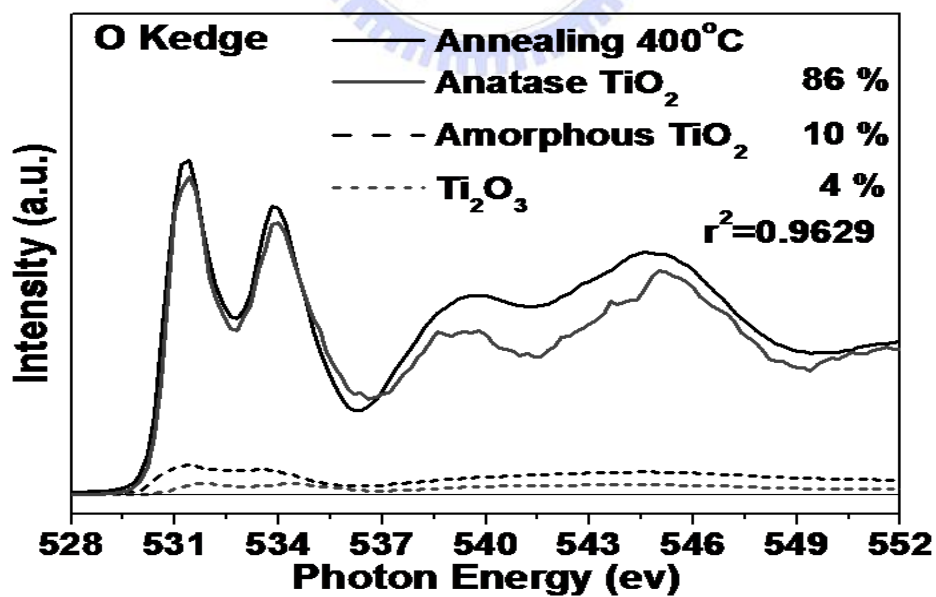
Figure 4-14   Fitting results for O K-edge XANES spectrum of TNAs annealed at 400° C

Table 4-3   Fitting results for the amount of crystalline and amorphous phases and impurities of TNAs as-grown in NH$_4$F solution and followed by post annealing at 400°C, and laser annealing with fluences of 0.042 Jcm^{-2}, and 0.1 Jcm^{-2} at 9000 shots

Annealing conditions	Percentage of Polymorphs TiO$_2$ and impurities (%)			
	TiO	Ti$_2$O$_3$	Amorphous TiO$_2$	Anatase TiO$_2$
As-grown at 25°C	7	11	82	0
400 ^{o}C	2	3	9	86
F = 0.042 J.cm^{-2}	0	0	19	81
F = 0.1 J.cm^{-2}	0	0	10	90

4.5 The Improvement of Crystallinity and the Reduction of Surface Damage of TNAs Induced by Excimer Laser Treatment with new Experimental Mode

Experiments using the parallel mode, the laser beam irradiated perpendicularly to sample, and the sample was kept fixed (see Figure 4-15 (a)). The SEM results shown that the surface morphology of TNAs are significantly damaged with fluence is higher than 0.133 Jcm^{-2} or the number of shots is higher than 18000. It indicates that the damage of TNAs surface is considerable by using the parallel mode. Moreover, the multi-phase structure of TNAs after laser treatment is not suitable for applications. Therefore, the tilted mode has been designed to reduce surface damage as well as to improve crystallinity of anatase phase in TNAs after laser irradiation (see Figure 4-15 (b)). In this mode, the angle between laser beam and sample is set at α, and sample can turn around the axis d with a turning angle θ.
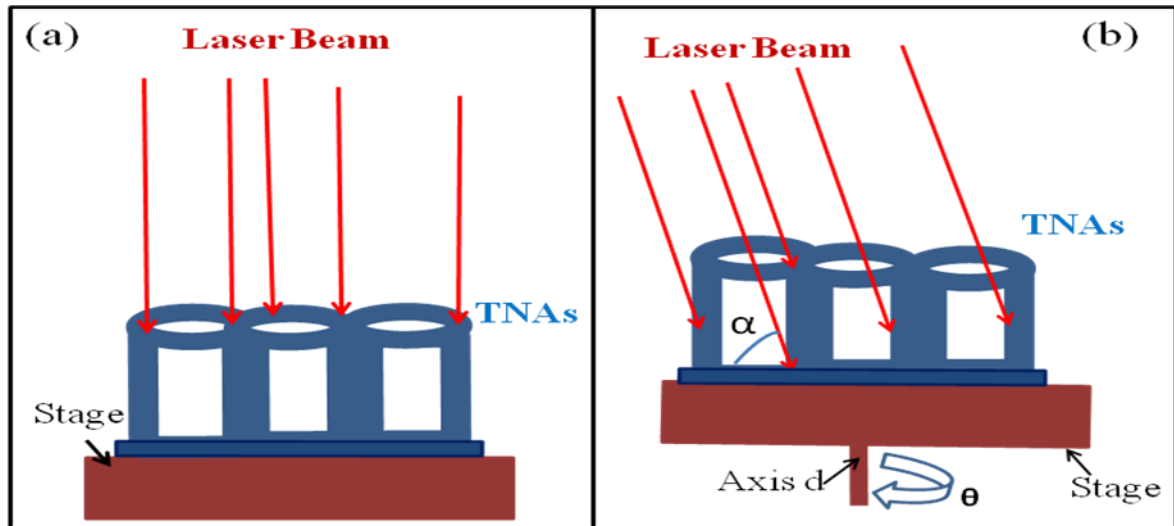
Figure 4-15   Schematic of experimental modes for laser anneal of TNAs/Ti samples: (a) parallel mode and (b) tilted mode.

A comparative study was carried out to distinguish any difference in surface morphology and crystallization of TNAs by laser annealing between parallel mode and tilted mode. The experimental parameters used in parallel and tilted mode are summarized in Table 4-4.

Table 4-4   The experimental parameters used in parallel and tilted modes

Mode	Parameters		Values								
Parallel mode	Fluence (Jcm^{-2})		0.125								
	α		90°								
	shots		9000								
Tilted mode	Fluence (Jcm^{-2})		0.125								
	α	case 1	60°								
		case 2	15°								
		case 3	5°								
	θ		0°	40°	80°	120°	160°	200°	240°	280°	320°
	shots		1000	1000	1000	1000	1000	1000	1000	1000	1000

The surface morphology of TNAs irradiated by laser in two modes is shown in Figure 4-16. As seen in the Figure 4-16 (a), the sample was irradiated by laser in parallel mode; the tubes were destroyed and melted together. As a result, the melting layer was formed on the top of nanotube arrays. When TNAs irradiated by laser in tilted mode at 60° or 15° of tilted angle, (Figure 4-16 (b) and (c)), the damage of surface decreased. Further decrease tilted angle to 5°, the surface morphology of TNAs was only slightly affected by laser (Figure 4-16 (d)). A few tubes were broken but no melting layer was formed on the surface of tubes.

These results can be explained basing on the differences of laser irradiating process in parallel mode and tilted mode. In the parallel mode, 9000 laser pulses were irradiated perpendicularly to surface of TNAs such that the top surface of tubes was accumulated a large energy in a short duration which resulted in damage and melting. On the other hand, in the tilted mode, with the angle between laser beam and sample was set at 5°, so the angle between laser beam and tubes is 85°. Thus, most laser beam was irradiated on the wall of TNAs. Hence, the surface morphology of TNAs was only slightly affected. Moreover, during laser irradiation, laser beam was not focused on one side of tubes. Instead the whole tubes were irradiated by laser beam such that any damage of TNAs could be minimized. Hence, 5° or smaller angle could be chosen for tilted angle to minimize the damage of surface of TNAs.

When TNAs samples were irradiated by laser in tilted mode, exist of broken tubes can due to the number of shots using for each turning time is large (1000 shots). Thus, several experiments have been carried out with the number of shots used for each turning time was deceased. The TNAs sample was irradiated by laser in tilted mode at 5° of tilted angle, 5° of turning angle and the 125 shots used for each turning time has surface morphology with almost no damage (Fig. 4-17).
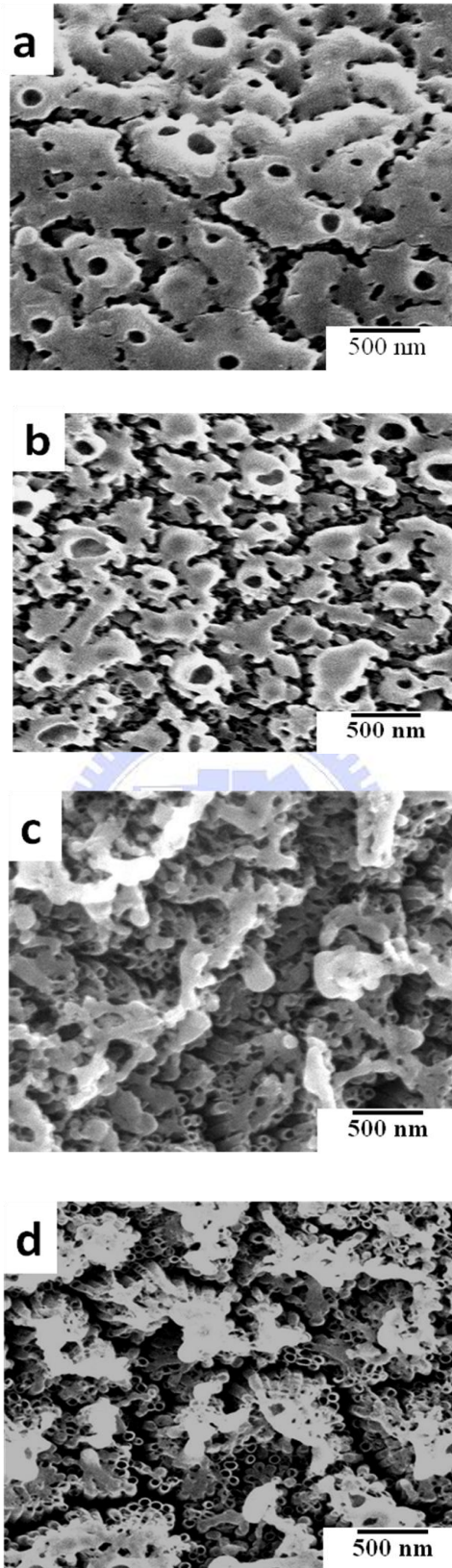
Figure 4-16   Surface morphology of TNAs annealed by laser in (a) parallel mode, tilted

mode at tilted angle of (b) 60°, (c) 15°, and (d) 5°.
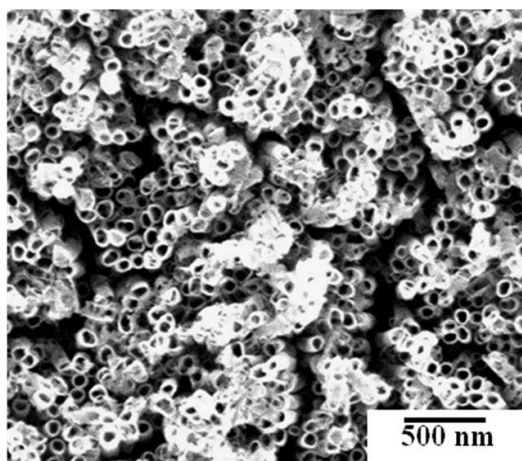
Figure 4-17   Surface morphology of TNAs annealed by laser in tilted mode at tilted angle

5°, and turning angle at 5°.

The decrease number of shots for each turning time is one of reasons to eliminate the

damage of TNAs. The as-grown amorphous TNAs have very low hardness, so when TNAs

were irradiated by laser with large the numbers of shots leading to TNAs were broken. On the

other hand, with small number of shots, TNAs could remain their shape and then transformed

to crystalline phases with higher hardness. In a result, TNAs were transformed from

amorphous to crystalline phases and the damage of tubes was eliminated.

In addition, ELA in tilted mode can also improve the crystallinity of TNAs. Figure 4-

17 shows the XRD spectra of TNAs irradiated by laser in parallel mode and tilted mode at 5°

of tilted angle with fluence of 0.125 J.cm^{-2} and 9000 of total shots. As shown in Figure 4-17,

the strong anatase (A) A(101) and A(200) peaks appear in XRD spectra of the TNAs/Ti

samples, and no rutile peaks can be observed. It indicates that TNAs amorphous is

transformed to anatase under these laser annealing conditions. Furthermore, the intensity of

A(101) peak of TNAs/Ti samples treated in tilted mode is higher than parallel mode. It

indicates that the crystallization of TNAs used in tilted mode is better than parallel mode.

Using equation (4) in Section 4.3, the weight percentages of anatase phase in TNAs samples

laser treated in parallel mode and tilted mode were summarized in Table 4-5. Parallel mode

yields 39.4 wt % of anatase phase, while tilted mode yields a much higher 74.8 wt % of anatase phase.

This contrasting result might be explained as follows. When TNAs were treated by laser in parallel mode, the energy of laser beam was transferred from the top to bottom of TNAs. Therefore, the top of tubes was transformed from amorphous to anatase first, then it continuously absorbed energy of laser beam and increase its temperature. The phase transformation of TNAs in the bottom was slow due to the heat conduction from top to the bottom. Yet, the accumulated energy at the top surface led to rutile phase and maybe melting and damage. On the other hand, in the tilted mode, almost laser beam was irradiated onto the wall of TNAs. In addition, TNAs were turned from 0° to 320° such that the whole tubes received energy of laser beam. As a result, all tubes could be crystallized homogeneously. Therefore, the crystallinity of anatase TNAs in tilted mode is improved.
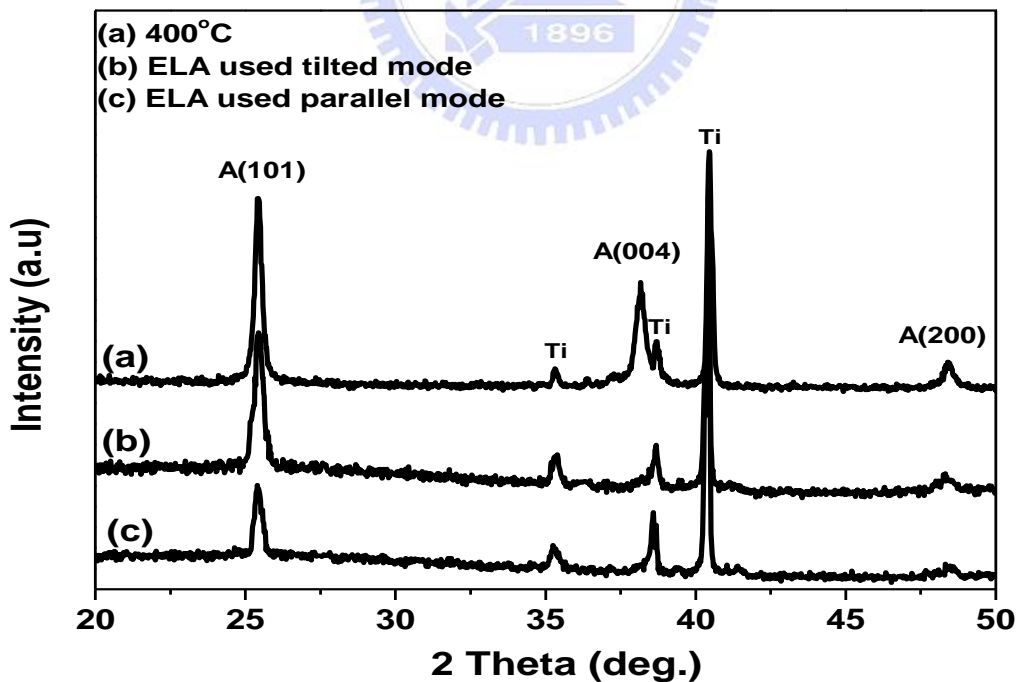
Figure 4-18   The XRD spectra of TNAs/Ti samples irradiated by laser using parallel mode and tilted mode, and post-annealed by furnace at 400^oC

Table 4-5   The anatase X-Ray peaks intensities and weight percentage of anatase in TNAs samples annealed by laser using parallel mode and tilted mode

Annealing conditions	Peaks intensities	Weight percentage (%)
	I_A	A
400^0 C, 1 hr	243.0	86.0
Tilted mode	211.4	74.8
Parallel mode	111.2	39.4

4.6   The Explanation of Microstructure and Surface Morphology Modification of TNAs Induced by Laser annealing

In this section, the mechanism of the crystallization of TiO_2 material induced by laser irradiation and the heat transfer in TNAs during laser annealing in parallel and tilted modes will be discussed.

First, the basic mechanism of laser heating process is through photon absorption and the subsequent rapid transfer of energy from the electrons to the lattice. During laser annealing a beam of photons is focused on a sample. Simply put, the photons interact with the electrons in the sample which then transfer the energy to the lattice. This causes localized heating in the area where the photons hit the sample.

More specifically, the wavelength of laser determines how the energy of laser will be absorbed in the TiO_2 material. The incident photon energy is determined by the equation:

$$E = hc/\lambda$$

with h equal to Planck's constant, c equal to the speed of light, and λ equal to the wavelength of the laser. With KrF (248 nm) excimer laser, the photon energy E equals to 5 eV. Furthermore, the photon energy of KrF excimer laser beam is 5 eV, which is larger than the fundamental band gap (E_g) of TiO_2 (3.5 eV for anatase, 3.2 eV for TiO_2 rutile, and 3.3 to 3.5

eV for amorphous phase [89]). Thus, the absorption of excimer laser excites the electrons from occupied to unoccupied energy states. These excited electrons have a kinetic energy of $\Delta E > 1eV$ such that they can move in the lattice, transfer their energy to other electrons, and excite them to become next excited electrons. The excited electrons also transfer energy to lattice leading to oscillation of lattice. Besides that, atoms and lattice can receive directly energy from the photons beam and start vibrating. Therefore, the interaction between light and matter is a combination of various processes including electrons, atoms (or vacancies) and phonons, which contribute to the heating of the lattices of sample. When the heating is sufficient, phase transitions may occur. In order to transform amorphous to anatase TiO_2, it is necessary to overcome an activation energy ($E_{\alpha-A}$) of 137 kJ/mol [64]. However, higher activation energy (E_{A-R}), from 350 to 500 kJ/mol [65-66] is required to enable the phase transition from anatase to rutile.

The effect of fluence on TNAs at 9000 shots can be explained as follows. When fluence is less than 0.133 Jcm^{-2}, the sample received thermal energy from laser E_L is higher than $E_{\alpha-A}$ and $E_L < E_{A-R}$, so amorphous TiO_2 is only transformed to anatase. When the fluence is higher than 0.133 Jcm^{-2}, the E_L is larger than E_{A-R}. Therefore, amorphous TiO_2 is transformed to anatase, and then further transformation to rutile TiO_2. When the fluence is further increased, higher E_L leads to increased amount of anatase and rutile TiO_2. Since the laser beam is directed at the top of TNA in parallel, the laser energy is transferred from top to bottom of tubes, leading to enhanced surface damage as E_L increases. Moreover, the surface of TNAs received larger energy from laser, so the damage of tubes occurred only on surface of TNAs.

For the study of the effect of shots on TNAs at 0.1Jcm^{-2} of fluence, when number of shots is less than 9000, thermal energy absorbed by TNAs over activation energy $E_{\alpha-A}$, so amorphous TiO_2 is transformed to anatase. In contrast, when number of shots is greater than 9000, the E_L is also higher than E_{A-R}. Thus, TiO_2 amorphous is transformed to anatase and rutile. In

addition, when number of shots is further accumulated, increased laser energy, E_L increases the amount of anatase or rutile TiO_2, and surface damage.

Second, the heat transfer in TNAs during laser annealing can be explained through investigation of the temperature T of samples. In this case of a TNAs–Ti substrate system, when the thickness of the TNAs cannot be neglected, T is given by [90]:

$$T(z,t) = [\frac{(1-R)I}{k_1}][(4\chi_1 t)^{1/2} \sum \xi^{|n|} ierfc[\frac{|z-2nh|}{(4\chi_1 t)^{1/2}}]] \tag{13}$$

$$\xi = \frac{k_1(\chi_2)^{1/2} - k_2(\chi_1)^{1/2}}{k_1(\chi_2)^{1/2} + k_2(\chi_1)^{1/2}} \tag{14}$$

In these equations, I is the effective fluence by unit time (expressed in W cm^{-2}). In the case of a semiconductor, $I = F(E-E_g)/E$. The factors k_1 and k_2 are the thermal conductivities of the film and the substrate, respectively; χ_1 and χ_2 are the heat diffusivities of the film and the substrate, respectively; z is the distance from the film–air interface; t is the time.

$$T(z,t) = F[(4\chi_1 t)^{1/2} \sum \xi^{|n|} ierfc[\frac{|z-2nh|}{(4\chi_1 t)^{1/2}}]][\frac{(1-R)}{k_1}\frac{E-E_g}{E}] \tag{13-1}$$

With TNAs/Ti samples and KrF (248 nm) excimer laser, the parameters k_1, χ_1, E, R are constants. Therefore, temperature T = T (z, t, F).

Considering the function $g = erfc[\frac{|z-2nh|}{(4\chi_1 t)^{1/2}}]$, it will obtain the maximum value at z = 0, and the increasing of z leads to the decreasing of function g. It indicates that the temperature T of sample (eq. 13-1) is maximum at the surface of the sample (z = 0) and its magnitude will decrease inside sample.

In the parallel mode, the laser beam was irradiated directly to surface of TNAs, so the temperature T of sample is a function of the depth z. T has maximum value at surface of TNAs (z = 0), and it will decrease with the increasing of z. It suggests that the heat transfer is function of depth. The surface of TNAs was absorbed energy of laser beam first and stared

54

transforming from amorphous to crystalline phases. The thermal energy was continued diffusing vertically inside sample. It implies that maybe the multilayer structure of TNAs was formed after laser treatment. Furthermore, after the crystalline phases formed on the surface of sample, they also continued absorbing energy of laser leading to the prevention of energy transfer into TNAs. It can explain the limitation of crystallinity of samples annealed by laser in parallel mode. In addition, in this mode, 9000 laser pulses were irradiated perpendicularly to surface of TNAs such that the top surface of tubes was accumulated a large energy in a short duration which resulted in damage and melting.

On the other hand, in the tiled mode, the laser beam was irradiated to the wall of TiO_2 tubes. The thickness of tube wall is only 20 nm, so the energy of laser could transfer through wall and crystallize it. When TNAs was turned with turning angle θ, the other side of tubes was crystallized by laser. Because the sample turned around the axis d from 0° to 360°, so laser beam scanned entire TiO_2 tubes. Hence, all tubes could be crystallized uniformly. Therefore, the crystallinity of TNAs in tilted mode is improved. In addition, laser beam was irradiated on the wall of TNAs, so the surface morphology of TNAs was only slightly affected. Moreover, the using small number of shots for each turning time is one of reasons to eliminate the damage of TNAs. The as-grown amorphous TNAs are week, so when TNAs were irradiated by laser with large shots number leading to TNAs were destroyed. On the other hand, with small laser shots number, TNAs could remain their shape and then transformed to crystalline phases with higher hardness. In a result, TNAs were transformed from amorphous to crystalline phases and the damage of tubes was eliminated.

In the conventional annealing by means of furnace, it typically takes minutes to hours to obtain phase transition at high temperature around 600^oC [15]. In the low-temperature excimer laser annealing, the transformation takes about 2 x 10^{-4} second, which is several orders of magnitude faster. The essence of such huge discrepancy can be attributed to the electronic effect. Indeed, the transformation of amorphous to crystal requires the

rearrangement of covalent bonds. This can be only achieved via creation, migration, and recombination of dangling bonds sites [91], which lead to a strong increase in the entropy of the transformation as well as to a sharp decrease in the formation and migration energies of dangling bonds. As a result, the crystal formation rate increases substantiality.

Chapter 5 Conclusions and Suggestions for Future Work

5.1 Conclusions

In this thesis, the effects of ELA on microstructure, electronic structure of TNAs prepared by anodic oxidation in NH_4F solution are investigated and analyzed. The transformation mechanism of TNAs amorphous into an anatase or rutile by eximer laser annealing at various annealing conditions has been proposed. TNAs irradiated by laser with fluences between 0.067 and 0.133 Jcm^{-2} under 9000 shots, will receive sufficiently a thermal energy to overcome the activation energy for transformation of amorphous to anatase. Besides, under ELA with fluence is higher than 0.133 Jcm^{-2} at 9000 shots or shots is greater than 9000 at 0.1 Jcm^{-2} of fluence, the TNAs obtained energy is higher than activation energy for anatase to rutile transformation leading to phase transition from amorphous TiO_2 to anatase and rutile. We also propose that electronic effects play a major role for observed crystallization. In addition, surface morphology appears to be strongly modified for TNAs irradiated by laser with fluence is higher than 0.133 Jcm^{-2}, or shots are greater than 9000. This research also introduced a simple and reliable method to determine structural characteristics and phase proportions with quantifiable numerical accurateness from the experimental data itself.

In this study, the self- organized TiO_2 nanotube arrays with high-aspect-ratio of 100:1 was prepared by anodic oxidation in ethylene glycol/water containing NH_4F. However, XANES results showed that large impurities of 18 % (11 % Ti^{3+} (Ti_2O_3), and 7 % Ti^{2+} (TiO) cations) and 82 % TiO_2 amorphous exist in as-grown TNAs. In order to obtain attractively applications of TNAs, the impurities Ti_2O_3 and TiO must be transferred to TiO_2. ELA technique is suitable for that because of impurities Ti_2O_3 and TiO were completely transferred to TiO_2 after laser treatment even at low laser fluence of 0.042 Jcm^{-2}. Furthermore, percentage of anatase TiO_2 rose to 90 % under ELA at 0.1 Jcm^{-2} of fluence. It indicates that ELA

technique might transfer all of impurities Ti_2O_3 and TiO in TNAs to TiO_2 as well as improve the phase transition from amorphous to anatase phase.

When the laser beam irradiated perpendicularly to sample, the problems appeared such as the surface morphology of TNAs was strongly modified and the phase transformation from TiO_2 amorphous into anatase phase was limited. Because of the heat transfer is function of depth. The surface of TNAs was absorbed energy of laser beam first and stared transforming from amorphous to crystalline phases. After the crystalline phases formed on the surface of sample, they also continued absorbing energy of laser leading to the prevention of energy transfer into TNAs. It can explain the limitation of crystallinity of samples annealed by laser in parallel mode. In addition, in this mode, 9000 laser pulses were irradiated perpendicularly to surface of TNAs such that the top surface of tubes was accumulated a large energy in a short duration which resulted in damage and melting. To solve these problems, the tilted mode has been designed to eliminate surface damage as well as to improve crystallinity of TNAs after laser irradiation. In the tiled mode, the laser beam was irradiated to the wall of TiO_2 tubes. Because the sample turned around the axis d from 0° to 360°, so laser beam scanned entire TiO_2 tubes. Therefore, the TNAs were crystallized homogeneously. In addition, laser beam was irradiated on the wall of TNAs, so the surface morphology of TNAs was only slightly affected. Moreover, the using a small number of shots for each turning time can avoid the damage of TNAs. Because the as-grown amorphous TNAs are week, so with small number of shots, TNAs could remain their shape and then transformed to crystalline phases with higher hardness. In a result, TNAs were transformed from amorphous to crystalline phases and the damage of tubes was eliminated.

In conclusion, high crystalline TiO_2 nanotube arrays were successfully obtained by using excimer laser annealing technique. Moreover, the excimer laser annealing technique performs at low-temperature and during short duration. Therefore, ELA is profitable

technique to optimize the structural phase of TiO_2 at low-temperature for applications such as flexible devices or sensors.

5.2 Suggestions for Future Work

The disadvantage of Lambda Physik Complex 201 excimer laser system used in this study is to create small laser pulses and its energy distribution is not homogeneous (Figure 27). As seen in Figure 27, almost energy of pulse exists in the center of pulse, energy of pulse distributes in surrounding zones is small. It is difficult to irradiate homogeneously to a large area of sample and damage the partial area of sample in the center of pulse. Therefore, in the future works, we will concentrate on setup of an excimer laser annealing system for creation the modeling laser beam homogenization is able to avoid the damage partial area of sample and can use for large sample.

The experimental setup of this excimer laser annealing system is shown in Figure 1. The laser annealing system includes a KrF pulsed excimer laser, beam delivery optics, chamber, and translation stage. A KrF (248 nm) excimer laser was used as a light source for the laser annealing system. The sample was placed in a chamber. The environment in the chamber is either vacuum or filled up by gas. A shaped and homogenized beam of the pulsed excimer laser was gone into the chamber through a quartz window and scanned over the surface of the sample. The purpose of using laser beam homogenizer here is to expand and shape homogenously line beam to realize easy scanning of entire sample surface.

The operating mechanism of Imaging Homogenizer is described in Figure 28. The Imaging Homogenizer is built from two microlens arrays (LA$_1$, LA$_2$) and one spherical lens, Fourier lens (FL) [92]. The plane of homogenization lies in the focal plane of the Fourier lens. As with homogenizer, the incident beam is split into many small sub beams with the first microlens array. The second microlens array then acts, in combination with the spherical lens,

like an array of objective lenses, overlapping the sub beams of the first array in the plane of homogenization. As the size of the flat top depends in this case on the distance between the two arrays, it can easily be adjusted by moving the second array. However, great care has to be taken that the second array is not moved into the focus plane of the first array, where it could be damaged by focussed high energy laser light. The Imaging Homogenizer usually uses microlens arrays of identical pitch. The shape of the flat top is determined by the shape of the microlenses.
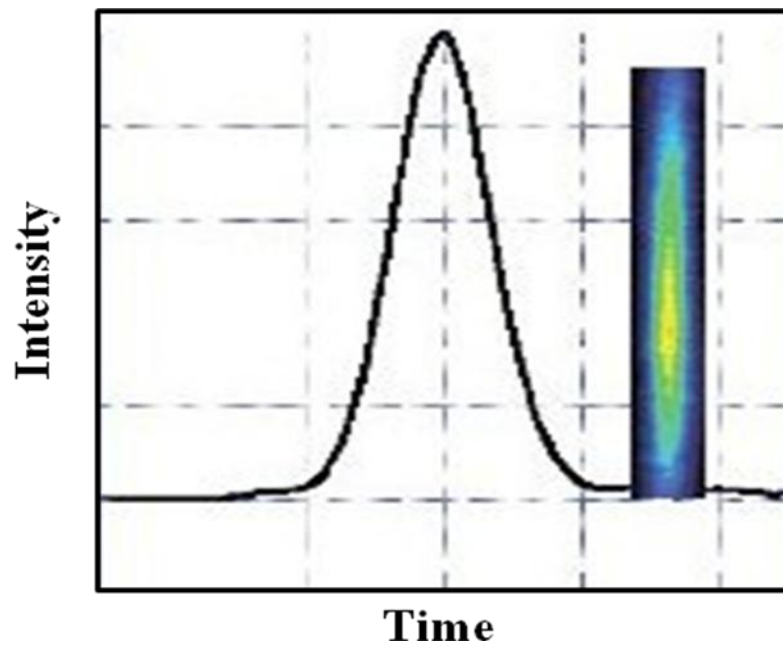

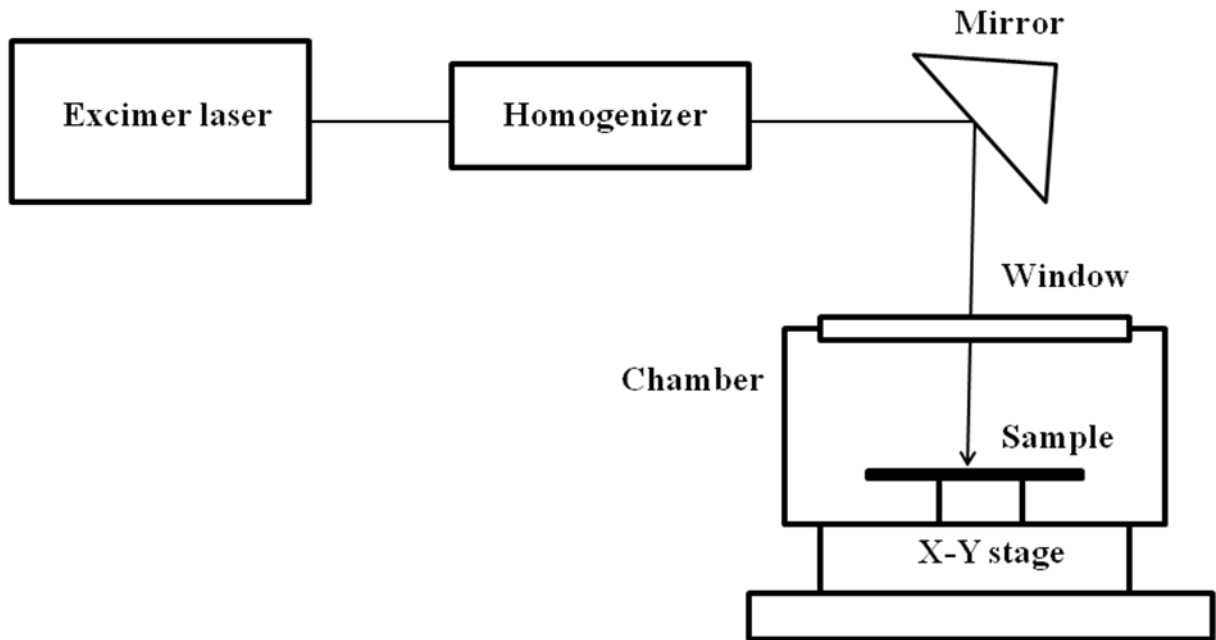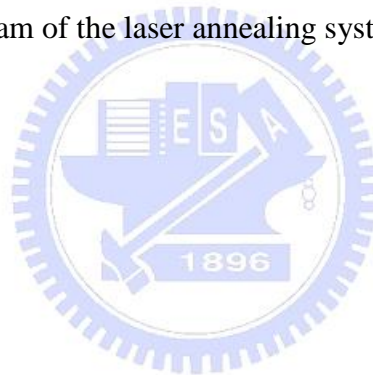Figure 5-1   Schematic diagram of original laser beam profile

Figure 5-2   Schematic diagram of the laser annealing system
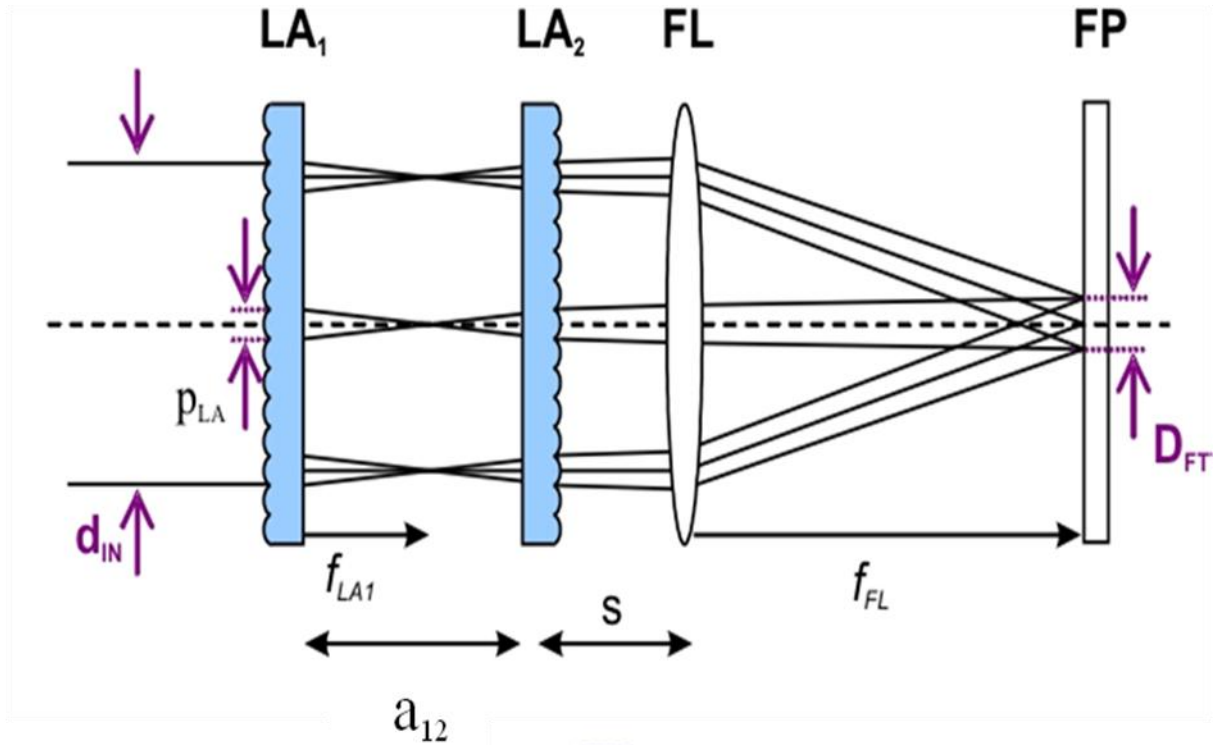
Figure 5-3   Schematic diagram of Imaging Homogenizer system [92]
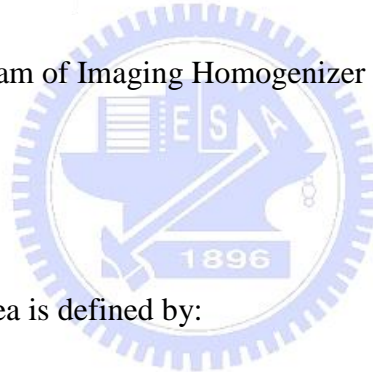
The size of the homogenized area is defined by:

$$D_{FT} = \frac{P_{LA_1} \cdot f_{FL}}{f_{LA_1} \cdot f_{LA_2}} [(f_{LA_1} + f_{LA_2}) - a_{12}]$$

With $f_{LA_1} < a_{12} < f_{LA_1} + f_{LA_2}$

As a result, the beam profile at the substrate plane is a "top hat" intensity distribution in both directions with long axis plateau uniformity, see Figure 30. After that the line beam is scanned across sample surface to produce uniform annealing whole sample (As seen in Figure 31).
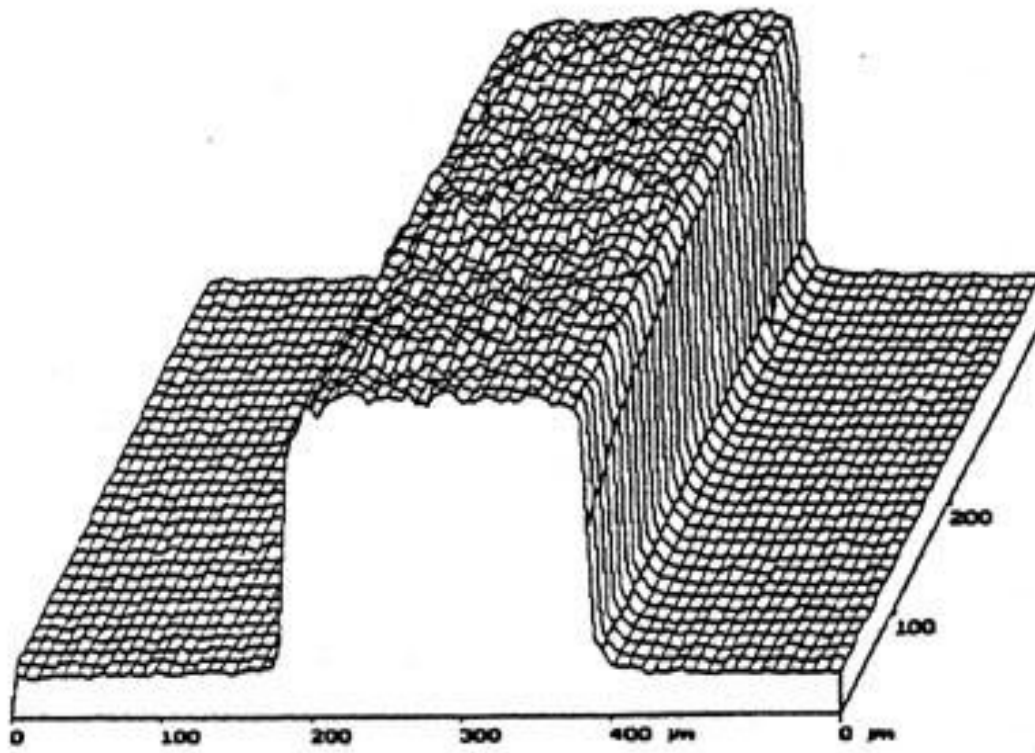
Figure 5-4   Line–shaped and homogenized of laser beam
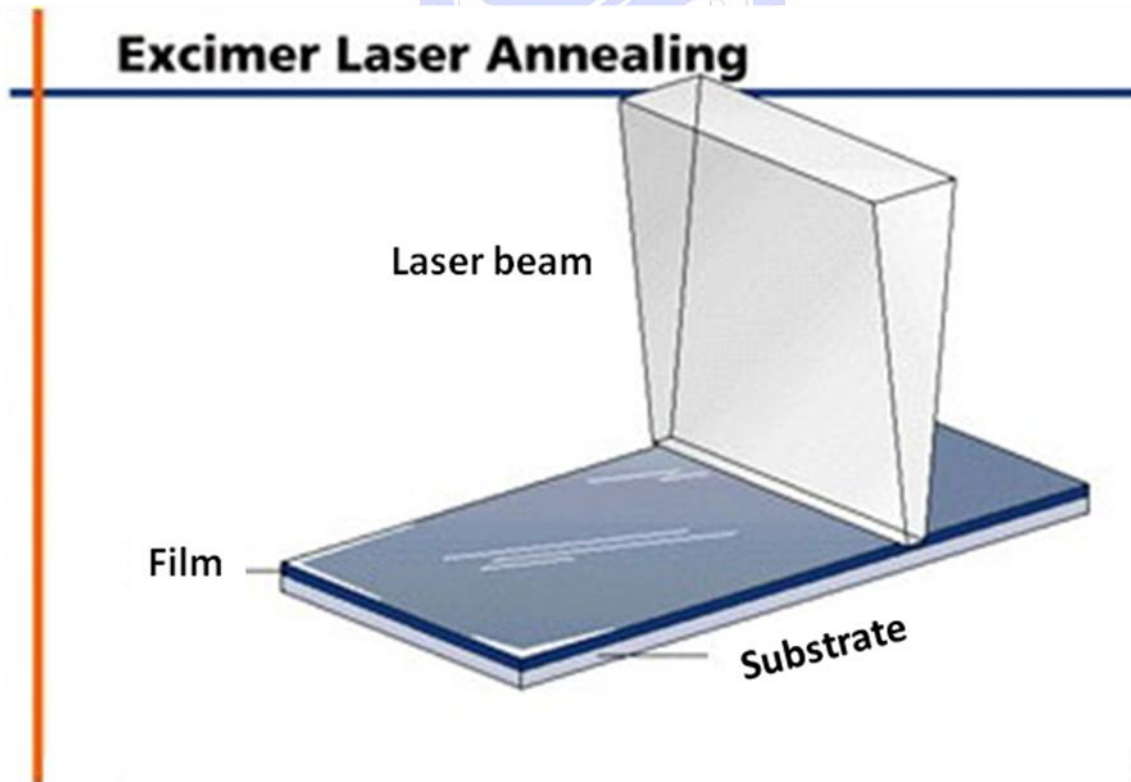
Figure 5-5   Schematic diagram of scanning excimer laser annealing

The excimer laser system has been introduced to homogeneously anneal large sample. In this system, Imaging Homogenizer used to create a large, line-shaped, homogenized laser beam. The beam profile at the substrate plane is a "top hat" intensity distribution in both directions with long axis plateau uniformity. Moreover, basing on the relative movement between line beam and X-Y stage, the line beam can scan entire sample surface to produce uniform annealing whole sample.

References

[1]   S. Y. Lin, Y. C. Chen, C. M. Wang, C. C. Liu, J. Solid State Electrochem. 12 (2008) 1481.

[2]   X. Z. Li, H. Liu, L. F. Cheng, H. J. Tong, Environ. Sci. Technol. 37 (2003) 3989.

[3]   O. K. Varghese, G. K. Mor, C. A. Grimes, J. Nanosci. Nanotech 4 (2004) 733.

[4]   B. O'Regan, M. Gratzel, Nature, 353 (1991) 737.

[5]   J. Jinting, I. Seijia, W. Fumin, A. Motonari, J. Phys. Chem. B 110, 5 (2006) 2087.

[6]   M. Adachi, Y. Murata, J. Takao, J. Jiu, M. Sakamoto, F. Wang, J. Am. Chem. Soc. 126 (2004) 14943.

[7]   V. Zwilling, E. Darque-Ceretti, A. Boutry-Forveille, D. David, M. Y. Perrin, M. Aucouturier, Surf. Interface Anal. 27 (1999) 629.

[8]   J. M. Macak, H. Tsuchiya, P. Schmuki, Angew. Chem. Int. Ed. 44 (2005) 2100.

[9]   J. M. Macak, H. Tsuchiya, L Taveira, S. Aldabergerova, P. Schmuki, Angew. Chem. Int. Ed. 44 (2005) 7463.

[10]   M. Kaneko, I. Okura, Photocatalysis: Science and Technology; Springer-Verlag: Berlin, 2002.

[11]   J. G. Yu, H.G. Yu, B. Cheng, J. Phys. Chem. B 107 (2003) 13871.

[12]   H. Kominami, J. Kato, S. Murakami, Catal. Today, 84 (2003) 181.

[13]   B. R. Sankapal, M. Ch. Lux-Steiner, A. Ennaoui, A. Appl. Surf. Sci. 239 (2005) 165.

[14]   N. Negishi, K. Takeuchi, Mater. Lett. 38 (1999) 150.

[15]   H. Zhang, J. F. Banfield, Mater. Res. 15 (2000) 437.

[16]   T. I. Kamins, Mater. Res. Soc. Symp. Proc. 33 (1984) 109.

[17] J. S. Luo, W. T. Lin, C. Y. Chang, W. C. Tsai, J. Appl. Phys. 82 (1997) 3621.

[18] D. R. Chen, J. S. Luo, W. T. Lin, C. Y. Chang, P. S. Shih, Appl. Phys. Lett. 73 (1998) 1355.

[19] Z. Zhang, J. Zhu, D. Su, J. Liu, H. Shen, Y. Wang, L. Kang, J. Zhou, S. Yang, P. Wu Thin Solid Films 375 (2000) 172.

[20] S. Otani, M. Kimura, N. Sasaki, Appl. Phys. Lett. 63 (1993) 1889.

[21] M. Taga, H. Miyaka, T. Kobayashi, Jpn. J. Appl. Phys. 33 (1994) 1534.

[22] X. M. Lu, J. S. Zhu, X. F. Huang, C. Y. Lin, Y. N. Wang, Appl. Phys. Lett. 65 (1994) 2015.

[23] X. M. Lu, J. S. Zhu, W. S. Hu, Z. G. Liu, Y. N. Wang, Appl. Phys. Lett. 66 (1995) 2481.

[24] S. B. Xiong, Z. M. Ye, J. M. Liu, A. D. Li, C. Y. Chen, X. L. Guo, Z. G. Liu, Appl. Surf. Sci. 110 (1997) 124.

[25] R. Ishihara, P. Ch. V.D Wilt, B. D. V. Dijk, A. Burtsev, J. W. Metselaar, C. I. M. Beenakker. Thin Solid Films 427 (2003) 77–85.

[26] J. H. Kim, W. J. Lee, J. D. Kim, and S. G. Yoon, metals and materials international, 11 (2005) 285.

[27] Y. Oguri, R. E. Riman, H. K. Bowen, J. Mater. Sci. 23 (1988) 2897.

[28] B. Ohtani, Y. Ogawa, S. Nishimoto, J. Phys. Chem. B 101 (1997) 3746.

[29] R. Rodriguez-Talavera, S. Vargas, R. Arroyo-Murillo, R. Montiel-Campos, E. Haro-Poniatowski, J. Mater. Res. 12 (1997) 439.

[30]   M. Gopal, W. J. Moberly-Chan, L. C. De-Jonghe, J. Mater. Sci. 32 (1997) 6001.

[31]   A.W. Czanderna, C. N. R. Rao, J. M. Honig, Trans. Farad. Soc. 54 (1958) 1069.

[32]   R. D. Shannon, J. A. Pask, J. Am. Ceram. Soc. 48 (1965) 391.

[33]   E. M. Levin, H. F. McMurdie, American Ceramic Society, Columbus (Ohio). (1975).

[34]   J. I. Kroschwitz, M. Howe-Grant, Kirk Othmer encyclopedia of chemical technology. 4th ed. 24 (1997).

[35]   H. Zhang, J. F. Banfield, J. Phys. Chem. B 104 (2000) 3481.

[36]   C. A. Grimes, G. K. Mor, TiO_2 NT Arrays Synthesis, Properties, and Applications. Norwell, MA: Springer (2009).

[37]   H. D. Jiang, S. K. Kim, S. J. Kim, J. Nanopart. Res. 3 (2001) 141.

[38]   O. K. Varghese, X. P. Yang, J. Kendig, et al., Sense. Lett. 4 (2006) 120.

[39]   G.E.Thompson, Thin Solid Films 297(1997) 192.

[40]   A. Jaroenworaluck, D. Regonini, C.R. Bowen, R. Stevens, D.A. Macro, J. Mater. Sci. 42 (2007) 6729.

[41]   M.M. Lohrengel, Mater. Sci. Eng. R Rep. 11 (1993) 243.

[42]   G. K. Mor, O. K. Varghese, M. Paulose, N. Mukherjee, C. A. Grimes. J. Mater. Res. 18 (2003) 2588.

[43]   A. Pakes, G. E. Thompson, P. Skeldon, P. C. Morgan, Corros. Sci. 45 (2003) 1275.

[44]   K. C. Popat, M. Eltgroth, T. J. LaTempa, C. A. Grimes, T. A. Desai, Titania nanotubes: a novel platform for drug-eluting coatings for medical implants? Small 11 (2007) 1878.

[45] K. C. Popat, L. Leoni, C. A. Grimes, T. A. Desai, Biomaterials 28 (2007) 3188.

[46] L. Peng, A. D. Mendelsohn, T. J. LaTempa, S. Yoriya, C. A. Grimes, T. A. Desai, Nano Lett. 9 (2009) 1932.

[47] S. Liu, A. Chen, Coadsorption of horseradish peroxidase with thionine on TiO_2 nanotubes for biosensing. Langmuir 21 (2005) 8409.

[48] Y. Xie, L. Zhoua, H. Huang, Biosens. Bioelectron. 22 (2007) 2812.

[49] S. C. Roy, M. Paulose, C. A. Grimes, Biomater. 28 (2007) 4667.

[50] K. C. Popat, M. Eltgroth, T. J. LaTempa, C. A. Grimes, T. A. Desai, Biomater. 28 (2007) 4880.

[51] M. V. Allmen, Laser and Electron Beam Processing of Materials, Academic Press, New York, (1980).

[52] G. E. Wood, Melting Mode of Pulsed Laser Processing, Academic Press, New York, (1984).

[53] J. F. Ready, Effects of High Power Laser Radiation, Academic Press, New York, 1971.

[54] H. Kurz, Mater. Res. Soc. Proc. 74 (1987) 3.

[55] H. C. Cullis, N. G. Chew, J. M. Poate, P. Baeri, Phys. Rev. Lett. 49 (1982) 219.

[56] D. T. Devaud, Appl. Phys. Lett. 46 (1985) 844.

[57] J. W. Galvin, P. S. Peercy, Appl. Phys. Lett. 46 (1985) 644.

[58] A. A. Grigoropoulos, X. Xu, S. L. Taylor, H. K. Park, Int. J. Heat Mass Transfr. 36 (1993) 1219.

[59] W. Y. R. Ishihara, T. Hattori, M. Matsumura, Jpn. J. Appl. Phys. 34 (1995).

[60] S. T. P. L. E. Rehn, and H. Wiedersich, Surface alloying by Iom, Electron, and Laser Beams, 1985.

[61] G. F. J. M. Poate, and D. C. Jacobson, (1983).

[62] N. M. J. J. C. C. Fan, Mat. Res. Soc. Symp. Proc. 23 (1984) 9.

[63] X. M. Lu, J. S. Zhu, X. F. Huang, C. Y. Lin, and Y. N. Wang, Appl. Phys. Lett. 65 (1994) 16.

[64] P. Baltazar, V. H. Lara, G. C´ordoba, R. Arroyo, J Sol-Gel Sci Techn. 37 (2006) 129.

[65] S. R. Yoganarasimhan, N. R. Rao, Trans. Farad. Soc. 58 (1962) 1579.

[66] R. D. Shannon, J. A. Pask, J. Amer. Ceram. Soc. 48 (1965) 391.

[67] S. Otani, M. Kimura, and N. Sasaki, Appl. Phys. Lett. 63 (1993) 1889.

[68] L. Herbst, H. J. Kahlert, B. Fechner, U. Rebhan, R. Osmanow, Spie use 2 5004 (2002) 10.

[69] H. Pan, S. H. Ko, C. P. Grigoropoulos, N. Miller, E. E. Haller, and O. Dubon, Appl. Phys. A: Mater. Sci. Process. 94 (2009) 111.

[70] S. C. Chung, C. I. Chen, P. C. Tseng, H. F. Lin, T. E. Dann, Y. F. Song, L. R. Huang, C. C. Chen, J. M. Chuang, K. L. Tsang, C. N. Chang, Rev. Sci. Instrum. 66 (1995) 1655.

[71] M. F. D. Groot, J. Faber, J. M. Michels, M. T. Czyzyk, M. Abbate, J. C. Fuggle, Phys. Rev. B 48 (1993) 2074.

[72] R. Ruus, A. Kikas, A. Saar, A. Ausmees, E. Nommiste, J. Aaik, A. Aidla, T. Uustare, I. Martinson, Solid State Commun. 104 (1997) 199.

[73]   M. F. Ruiz-Lopez, A. Munoz-Paez, J. Phys: Condens. Matter. 3 (1991) 8981.

[74]   D. W. Fischer, Phys. Rev. B 5 (1972) 4219.

[75]   M. Yoshiya, I. Tanaka, K. Kaneko, H. Adachi, J. Phys. Condes. Matter, 11 (1991) 3217.

[76]   J. Verbeeck, S. V. Aert, Ultramicroscopy 101 (2004) 207.

[77]   G. Bertoni, E. Beyers, J. Verbeeck, M. Mertens, P. Cool, E. F. Vansant, G. V. Tendeloo, Ultramicroscopy 106 (2006) 630.

[78]   Taekon Kim, Crystallization of amorphous silicon thin films induces by nanoparticle seeds, Phd. D. Dissertation, University of Florida, 2009.

[79]   C. Ruan, M. Paulose, O. K. Varghese, G. K. Mor, C.A Grimes, J. Phys. Chem. B. 109 (2005) 15754.

[80]   Q. Cai, M. Paulose, O. K. Varghese, C. A. Grimes, J. Mater. Res. 20 (2005) 230.

[81]   L. Alexander, H. Klug, Anal. Chem. 20 (1948) 886.

[82]   R. A. Spurr, H. Myers, Anal. Chem. 29 (1957) 760.

[83]   R. Brodson, B.G. Williams, W. Engle, H. Sauer, E. Zeitler, J. M. Thomas, Solid Satate Commun. 64 (1987) 609.

[84]   L. Sonano, M. Abbate, J. Vogel, J. C. Fuggle, A. Fernandez, A. R. Gonzalez-Ehpe, M. Sacchi, J. M. Sanz, Surf. Sci. 290 (1993) 427.

[85]   V. S. Lusvardi, M. A. Barteau, J. G. Chen, J. Eng, B. Fruhberge, A. Teplyakov, Surfa. Sci. 397 (1998) 237.

[86]   E. Z. Kurmaev, R. G. Wilks, R. Filby, A. Moewes, L. Muller, F. A. Muller, Mater. Sci. Eng. C-Biomimetic. Supramol. Syst. 29 (2009) 136.

[87]   J. Biener, M. Baumer, J. Wang, R. J. Madix, Surf. Sci. 450 (2000) 12.

[88]   J. Biener, M. Baumer, R. J. Madix, Surf. Sci. 432 (1999) 178.

[89]   K. Eufinger, D. Poelman, H. Poelman, R. De Gryse, G.B. Marin, Appl. Surf. Sci. 254

        (2007) 148.

[90]   D. Bauerle, Laser Processing and Chemistry, Springer, Berlin, 2000

[91]   M. Wautelet, Semicond. Sci. Technol. 3 (1988) 54.

[92]   R. Voelkel, K. J. Weible, Spie Europe. Optical Systems Design (1998).